Numerical Simulation of Thunderstorm Outflow Dynamics. Part I: Outflow Sensitivity Experiments and Turbulence Dynamics

KELVIN K. DROEGEMEIER

School of Meteorology, University of Oklahoma, Norman, OK 73019

ROBERT B. WILHELMSON

Department of Atmospheric Sciences, University of Illinois, Urbana, IL 61801

ABSTRACT

In this first paper of a two-part series, a two-dimensional numerical model is developed and used to investigate the dynamics of thunderstorm outflows. By focusing only on the outflow and using essentially inviscid equations and high spatial resolution, we are able to explicitly represent important physical processes such as turbulent mixing. To simplify interpretation of the results, the model atmosphere used in all experiments is calm and dry adiabatic. This approach allows us to establish basic characteristics of modeled outflows in simple physical settings, and provides a foundation for future studies using more realistic environments.

All simulated outflows are initialized by prescribing a (controlled) horizontal flux of cold air into the model domain through a lateral boundary. In a series of sensitivity tests, we examine three parameters of the cold air source region: 1) the vertical temperature deficit profile, 2) the magnitude of the temperature deficit, and 3) the cold-air depth. By holding two of these quantities fixed while varying the third, we establish relationships among outflow speed, depth, and internal temperature deficit by comparing model results with laboratory density current experiments, inviscid fluid theory, and observations of thunderstorm outflows.

Our simulations indicate that the internal outflow head circulation is governed primarily by the outflow's vertical temperature distribution, and that this circulation plays a key role in determining the gust front propagation speed and outflow head depth. A pressure jump precedes the onset of cold air at the surface, and is shown to be dynamically induced by the collision of the outflow and environmental air masses at the gust front. In addition, the surface pressure distribution behind the outflow head is a consequence not only of hydrostatic effects, but also horizontal rotation aloft associated with a breaking head wave.

Turbulent mixing within the modeled outflows is associated with breaking Kelvin–Helmholtz billows which form at the shear interface atop the cold-air pool. These billows are qualitatively and quantitatively similar to turbulent eddies found in laboratory density currents, and are found to be sensitive to the magnitude of the computational smoothing as well as the grid resolution. Time-dependent air parcel trajectories are utilized to elucidate the kinematic structure of the simulated flow fields.

1. Introduction

The thunderstorm cold-air outflow, a region of evaporatively-cooled downdraft air which spreads out along the ground beneath a precipitating cloud, has long been recognized as a key component of convective storm dynamics. Outflows are known to trigger successive convective cells in multicellular storms (e.g., Wilhelmson and Chen, 1982; Miller and Fankhauser, 1983; Peterson, 1984), sustain supercell storms by enhancing low-level convergence (e.g., Brandes, 1977, 1984), and play a role in mesocyclogenesis and tornadogenesis (e.g., Brandes, 1981; Klemp and Rotunno, 1983; Rotunno and Klemp, 1985).

The interaction of a *gust front* (the leading edge of an outflow) with a dryline, a cold front, a seabreeze front, or another gust front is important in determining when and where convective clouds are likely to form (e.g., Purdom, 1976, 1979, 1982; Holle and Maier,

1980; Weaver and Nelson, 1982; Droegemeier and Wilhelmson, 1985a,b). Furthermore, outflows appear to be a key ingredient in promoting merger between existing clouds (e.g., Simpson et al., 1980; Tao and Simpson, 1984).

Figure 1 shows a schematic vertical cross section of the basic features of a mature outflow. The bold solid line depicts the transition zone between the cool outflow air and the warmer environment, while the arrows show the flow field relative to the gust front. As cold air approaches the front from within the outflow, much of it is deflected upward (counterclockwise) by a solenoidally induced circulation (Goff, 1975; Mitchell and Hovermale, 1977). Air closer to the ground turns downward under the influence of surface friction (marked "backflow" in Fig. 1). Warm environmental air approaching the gust front is forced over the cold-air pool, and often forms a shelf, roll, rope, or arc cloud. Under certain conditions, deep convection may be ini-
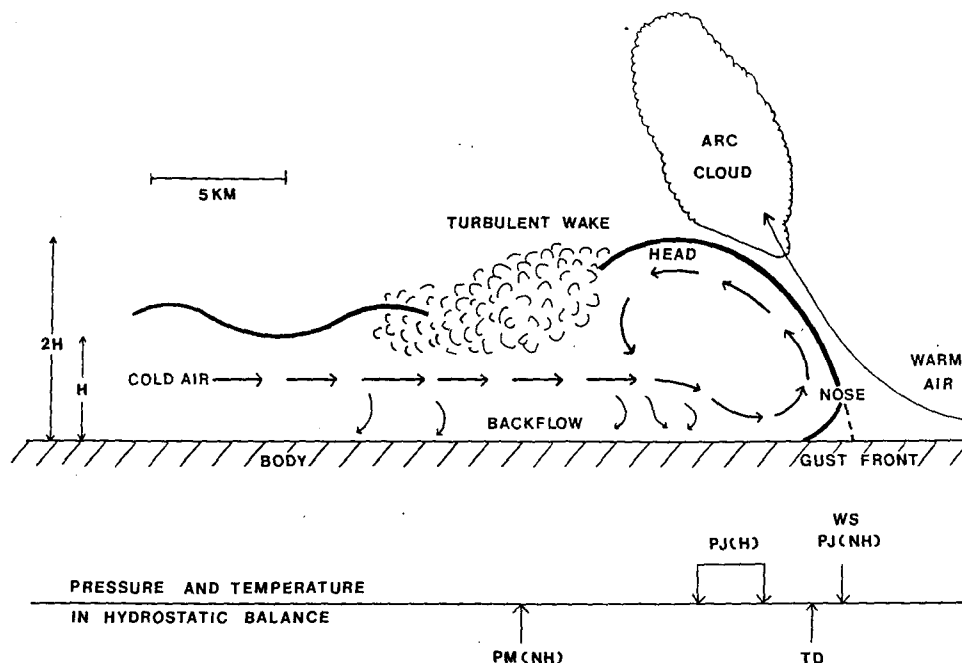
FIG. 1. Schematic vertical cross section through a mature thunderstorm outflow (vertical scale exaggerated), and the corresponding changes in surface meteorological parameters. See the text for details. (Adapted from Charba, 1974; Goff, 1975; Wakimoto, 1982; Koch, 1984).

tiated by this lifting (e.g., Wilhelmson and Chen, 1982; Droegemeier and Wilhelmson, 1985a,b).

Separating the body of the outflow from the elevated head is a turbulent wake. A protruding nose of cold air is hypothesized to exist at some gust fronts, and this feature is thought to periodically collapse and reform due to surface frictional influences (e.g., Charba, 1974; Goff, 1975).

Below the outflow schematic is shown the typical sequence of events at the surface that attend outflow passage (composited from Charba 1974; Goff, 1975; Wakimoto, 1982; Koch, 1984). Prior to the arrival of the cold air, the wind begins to shift (WS) and the pressure increases or jumps (PJ) due to a dynamic deceleration between the cold and warm air masses (Wakimoto, 1982). The passage of the cold air, often called the temperature break or drop (TD), is accompanied by a hydrostatic increase in pressure (PH). The surface pressure reaches a local minimum (PM) behind the outflow head due to dynamical effects of the mixed wake (section 4), while in the body of the outflow, the pressure and temperature are in quasi-hydrostatic balance.

Instrumented towers have been used to obtain high-resolution data on the kinematic and thermodynamic structure of outflows (e.g., Goff, 1975, 1977; Klingle, 1985). However, towers typically sample only the lowest 20 to 50 percent of most outflows, and such data represent only a single vertical cross section through a continually evolving, three-dimensional flow field. In light of these limitations, Doppler lidar and radar are

being utilized to study outflows (e.g., Wakimoto, 1982; Emmitt, 1985; McCaul, 1985; Fulton and Zrnić, 1985). Although capable of observing the entire three-dimensional structure of an outflow, radars often suffer significant antenna side-lobe problems when scanning close to the ground. Furthermore, since Doppler radar and lidar provide information only on the kinematics of the flow field (with lidar suffering from significant attenuation in the presence of moisture and clouds), the thermodynamic data, which are crucial in fully understanding outflow dynamics, are not readily available.

The dynamical similarity between thunderstorm outflows and density (or gravity) currents, established by Charba (1974), has allowed examination of many basic outflow properties with a laboratory tank apparatus (e.g., Keulegan, 1957, 1958; Middleton, 1966; Simpson, 1969, 1972, 1982; Simpson and Britter, 1979, 1980; Britter and Simpson, 1978, 1981; Didden and Maxworthy, 1982). Figure 2 shows a sequence of photos, spaced 1 s apart, of a laboratory density current (salt water, colored white) moving from left to right in a tank of fresh water (Simpson, 1969). Distinctly evident in this photo are multiple turbulent eddies resulting from Kelvin–Helmholtz (KH) instability at the upper density interface. These structures form periodically near the frontal region, and then grow in size until eventually breaking down into small-scale turbulence as a result of their own gravitational instability. Although comparisons have been drawn between outflows and density currents, many key issues remain to
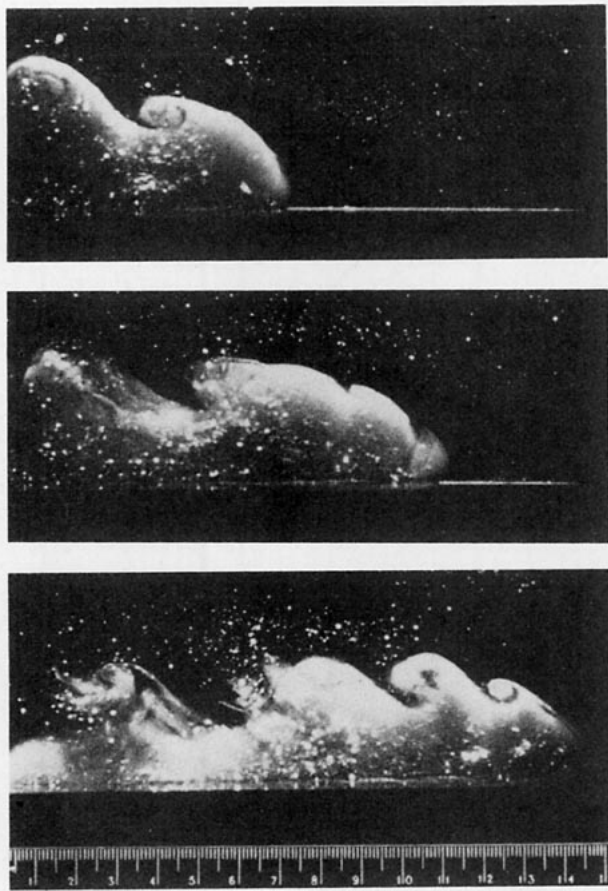
FIG. 2. Vertical cross sections at 1 s intervals through a laboratory density current (salt water, colored white) moving from left to right in a tank of fresh water. Slit lighting reveals multiple Kelvin–Helmholtz billows at the upper density interface. The scale at the bottom of the tank is in centimeters. See the text for further details. (From Simpson, 1969).

be addressed. For example, although turbulent eddies like those in Fig. 2 are almost always observed in laboratory tank flows, little effort has been expended to ascertain if similar features may be responsible for turbulence in outflows, or if such instabilities might influence the ability of air passing over the gust front to reach the parent storm updraft.

One of the most important contributions made by laboratory tank experiments has been the examination of the theoretical density front propagation speed (Benjamin, 1968):

$$V_f = (2gH\Delta\rho/\rho)^{1/2} \qquad (1)$$

where V_f is the propagation speed of the density front in a calm environment, $\Delta\rho$ is the positive density difference between the density current and the surrounding fluid (which has density ρ), and H is some characteristic depth of the density current (usually taken as the height of the following flow far behind the head region—Fig. 1). Note that (1) is strictly valid only for inviscid, incompressible, steady flows. Quite often, this equation is written

$$V_f = k(gH\Delta\rho/\rho)^{1/2} \qquad (2)$$

where k is a constant (the internal densimetric Froude number) which has a value of $\sqrt{2}$ for steady, inviscid flow. When applying (2) to the atmosphere, $\Delta\rho/\rho$ is typically replaced with $\Delta\theta/\theta$ (as in the discussions to follow) or $\Delta T/T$.

The accuracy of (2) in predicting the frontal speed of both laboratory density currents and thunderstorm outflows has been evaluated in several studies (Table 1). The value of k is typically found to be much less than $\sqrt{2}$, suggesting that the loss of momentum in the density current by turbulent mixing (Fig. 2), wave form drag, or surface friction is significant.

Seitter (1983) proposed the following modification to (2) for application to thunderstorm outflows:

$$V_f = k(\Delta P/\rho)^{1/2} \qquad (3)$$

where ΔP is the difference in *surface hydrostatic pressure* between the density current *head* and the ambient environment, and ρ is the environmental density. Seitter pointed out that, for constant density fluids, (2) and (3) give identical results. However, in contrast to true density currents, the density varies with height in thunderstorm outflows, and thus (3) is attractive because it takes into account the density difference integrated over the depth of the outflow head. In applying (3) to several simulations using a moist, two-dimensional numerical outflow model, Seitter obtained a mean value for k of 0.77.

Although laboratory tank experiments are useful for studying the basic properties of outflows, logistical considerations limit the realism of such studies. For example, it is difficult to include continuous stratification, low-level inversions, and ambient fluid shear in a laboratory setting. In addition, the sensitivity of laboratory density currents to the depth of the water tank makes direct application of the results to the atmosphere somewhat questionable. As a result, numerical models have been utilized to gain insight into outflow dynamics.

In the past 10 years, only a few investigators have attempted to numerically simulate thunderstorm outflows (Table 2). In the most detailed of these studies, Mitchell and Hovermale (1977) addressed several aspects of outflow dynamics with a dry, two-dimensional, slab-symmetric model. They initialized the outflow with a time-dependent heat sink designed to represent the evaporative cooling associated with thunderstorm downdrafts. Since the lateral boundaries of the model were rigid walls, no ambient environmental flow could be incorporated in their experiments.

Figure 3 shows vertical cross sections of potential temperature (K), horizontal velocity (m s^{-1}), vertical velocity (m s^{-1}), and the streamfunction (m^2 s^{-1}) at 12 min for Mitchell and Hovermale's reference simula-

TABLE 1. Values of the internal densimetric Froude number k from several laboratory, observational, and numerical experiments (adapted from Wakimoto, 1982).

Reference	k	Date source
Georgi (1936)	0.74	Pampero secco
Farquharson (1937)	0.90	Haboob
Keulegan (1958)	0.76 to 1.11	Laboratory experiments
Middleton (1966)	0.75	Laboratory experiments
Benjamin (1968)	1.1 to $\sqrt{2}$	Theory and laboratory experiments
Daly and Pracht (1968)	0.70	Numerical model
Simpson (1969)	0.72	Sea Breeze
Charba (1974)	1.25	Observed gust front
Wakimoto (1982)	0.77	Observed gust fronts
Seitter (1983)	0.77	Numerical model

tion. The bold dashed line in panels b, c, and d is the 314 K isentrope, a rough indication of the outflow boundary. In Fig. 3a, the outflow is advancing from left to right, away from the parameterized downdraft. In agreement with Fig. 1, an elevated head is evident at the gust front. However, there is no sign of turbulent mixing behind (upstream from) this region, even though Mitchell and Hovermale attributed looping of air parcel trajectories near the heat sink to this process.

The horizontal velocity field (Fig. 3b) shows a core of strong winds (maximum value of 28 m s^{-1}) which, due to surface friction, is located a few hundred meters off the ground. Also evident in Fig. 3b is strong horizontal return flow (maximum value of -10 m s^{-1}; dashed contours) in the ambient environment from just above the outflow to the top of the model domain. This return flow is artificially strong, and is largely a consequence of the model's rigid boundary conditions (Droegemeier, 1985).

In the vertical velocity field (Fig. 3c), a region of upward motion (maximum value of 10 m s^{-1}) is present at the gust front in agreement with the general flow

TABLE 2. Previous numerical outflow modeling studies.

Investigators	Approach
Mitchell and Hovermale (1977)	Dry, 2-D slab-symmetric model with rigid boundaries (heat sink).
Teske and Lewellen (1977)	Dry axisymmetric model with detailed turbulence parameterization.
Thorpe et al. (1980)	Dry 2-D slab-symmetric model with open lateral boundaries (heat sink).
Achtemeier (1982)	Semi-Lagrangian, 2½ dimensional model.
Seitter (1983)	Moist, 2-D slab-symmetric model (heat sink).
Addis (1984)	Dry, one-dimensional hydrostatic model.
Crook and Miller (1985)	Dry, 2-D slab-symmetric model with open lateral boundaries (undular bore study).

structure of Fig. 1. As documented by the streamfunction field in Fig. 3d, the magnitude of the vertical motions is exaggerated somewhat by the two-dimensionality of the model, and to a larger extent by the rigid boundary conditions. Consequently, due to mass continuity, a closed vertical circulation develops within the model domain. Except perhaps under conditions of neutral stability throughout the troposphere, one would not expect to see such a deep or intense circulation in the real atmosphere, and thus the model results must be viewed with some suspicion.

It is clear that limitations in observing tools, laboratory experiments, and computing techniques have denied a comprehensive investigation of thunderstorm outflow dynamics. Consequently, as part of a broad, long-range effort to improve our understanding of subcloud phenomena, we have developed a new high-resolution numerical model to investigate thunderstorm outflows. *The key objective of this study is to simulate outflows with very high spatial resolution in an attempt to explicitly depict the details of outflow morphology.* Since we are interested only in outflows and not their parent storms, we ignore the latter in this study and obtain the needed spatial resolution by initializing the outflows as horizontally propagating pools of cold air. Instead of employing real data to define the initial environment, we feel it is appropriate at this point to use rather idealized temperature and wind profiles. This not only simplifies interpretation of results concerning a phenomenon that is not yet well understood, but it also allows us to establish the basic characteristics of modeled outflows in *simple physical settings*. By systematically varying physical parameters such as wind shear and static stability in the model, we may easily span parameter spaces of outflow behavior. Later, more complex (i.e., realistic) experiments will be performed using observed data.

The model developed for this study (section 2) is designed with the versatility needed to address many questions concerning thunderstorm outflows. Those to be discussed in this paper include:

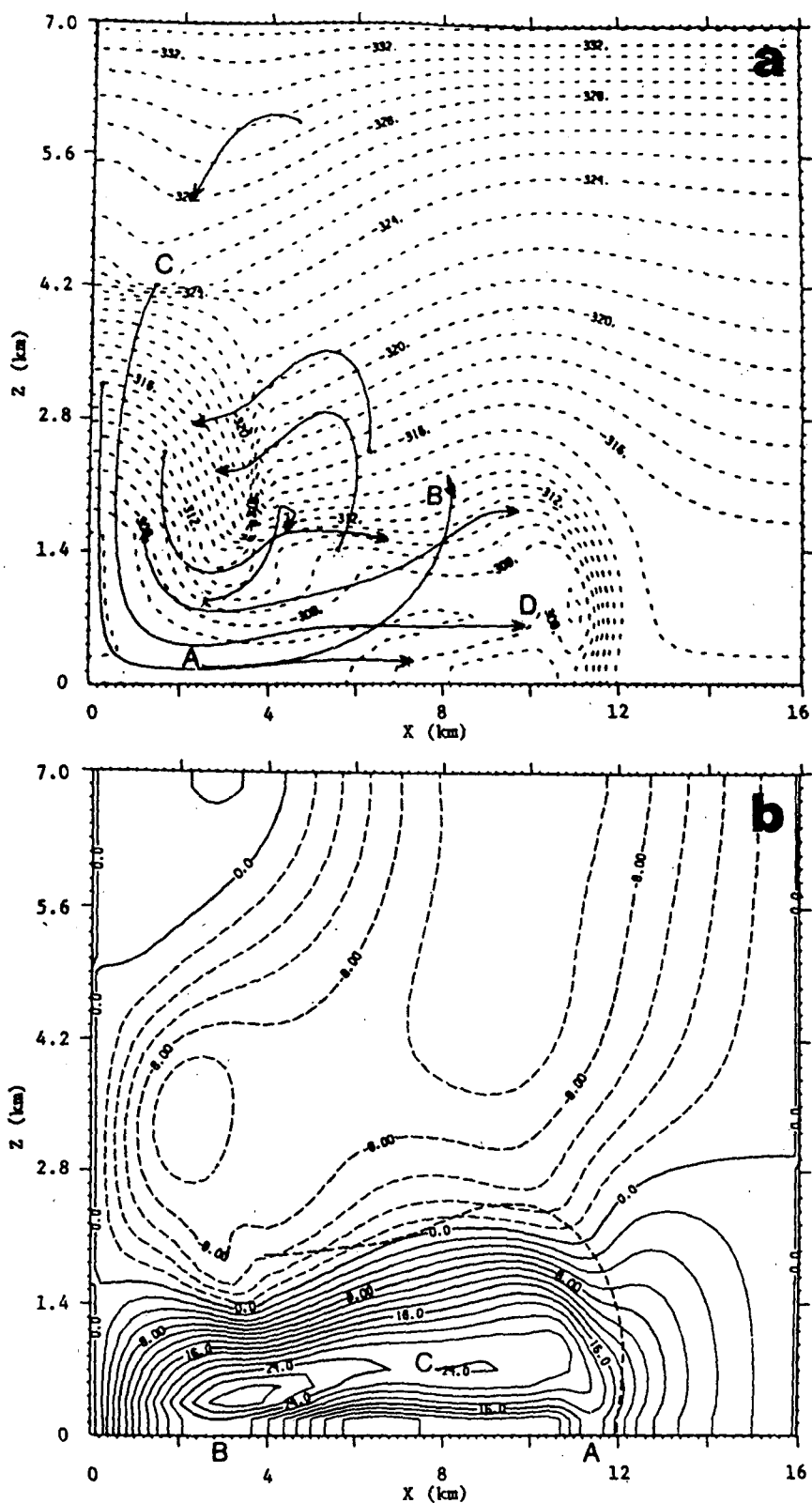1) What governs the depth of the outflow head (section 3)?

FIG. 3. Vertical cross sections at 12 min through a numerically simulated outflow showing (a) the potential temperature (deg K; dashed lines with a contour interval of 1 K), (b) the horizontal velocity (m s^{-1}; solid lines depict flow from left to right; contour interval of 2 m s^{-1}), (c) vertical velocity (m s^{-1}; solid lines denote upward motion; contour interval of 1 m s^{-1}), and (d) the streamfunction (m^2 s^{-1}; contour interval of 2 × 10^3). The arrows in panel a depict air parcel trajectories, and the dashed curve in panels b–d depicts the approximate location of the cold-air interface. (From Mitchell and Hovermale, 1977.)
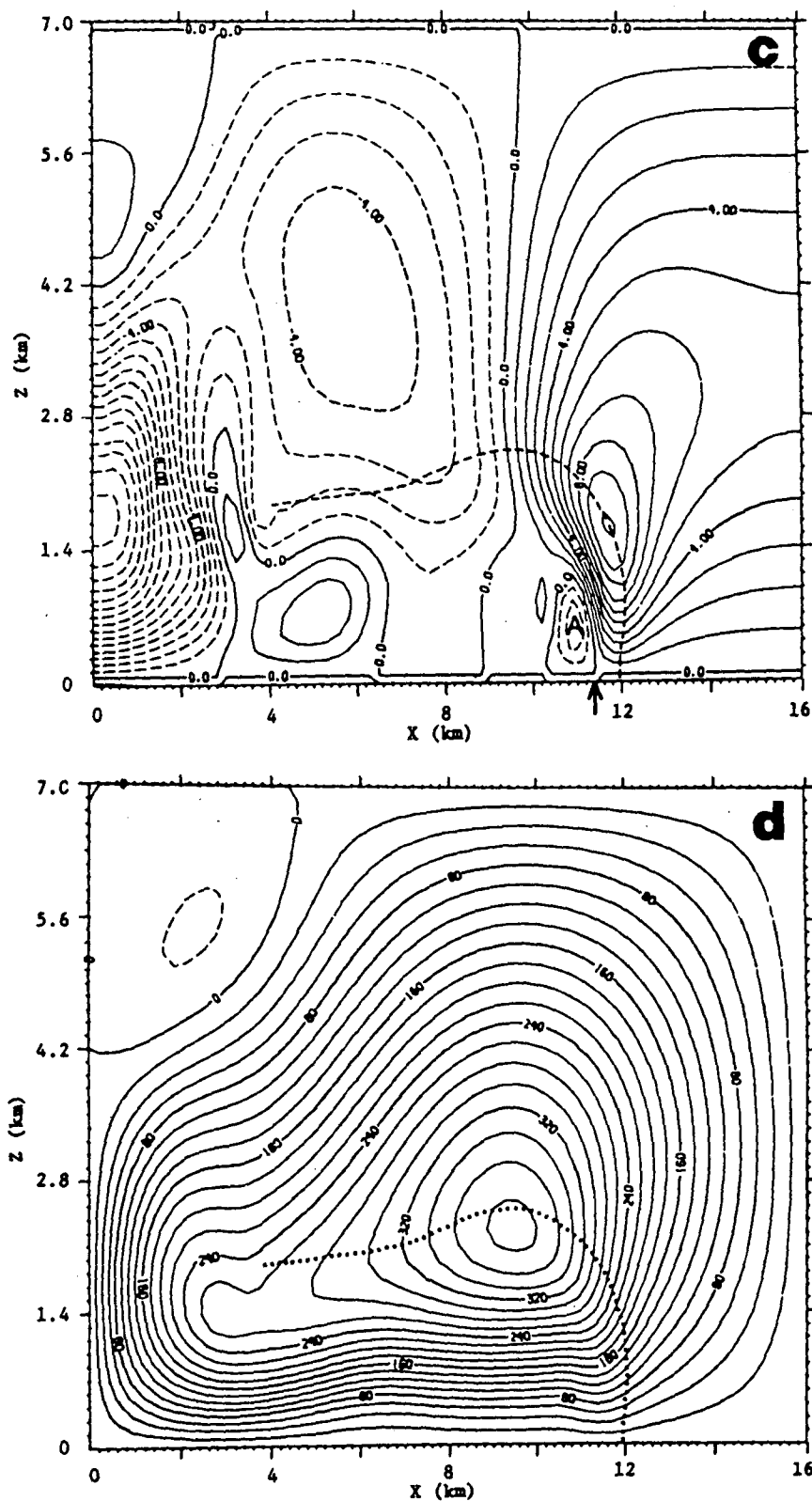
FIG. 3. (*Continued*)

2) What are the relationships between outflow speed, depth, frontal-induced convergence, and frontal lifting (section 3)?

3) To what extent is the environment ahead of an outflow influenced by the outflow itself (sections 3 and 4)?

4) What are the physical mechanisms of turbulence in outflows (section 4)?

5) How similar are outflows to laboratory density currents (section 4)?

Section 5 presents a summary of findings and comments on future research, and section 6 discusses a movie of our experiments which is available upon request.

Although the above topics by no means encompass all unanswered questions concerning outflows, they are meant to lay the foundation for future research. Part II of this paper will address the effects of ambient wind shear and static stability on outflow dynamics, and comparisons will be drawn between model results and outflows observed with Doppler radar.

2. The numerical outflow model

a. Model philosophy

The development of the numerical model is guided by the desire to simulate thunderstorm outflows with *high spatial resolution in an effort to resolve, rather than parameterize, physically important processes.* For example, one of the most important aspects of outflow and density current dynamics is turbulence (Fig. 2). In most numerical models, subgrid scale turbulence is parameterized using various closure techniques based on the turbulent kinetic energy, the local velocity deformation, or the vorticity. Unfortunately, such parameterizations are, at best, only crude approximations to true physical mixing processes. This is particularly true in two-dimensional models, like the one employed here, because much of the turbulent energy cascades in the wrong direction, i.e., upscale rather than downscale (Deardorff, 1975).

With these points in mind, a set of inviscid equations is adopted for the outflow model, and no turbulence closure scheme is used. Implicit in this approach is the assumption that the chosen grid resolution is adequate for depicting the turbulent features of interest, and that smaller scale motions are relatively unimportant (i.e., contain relatively little energy). Physically, this is not entirely true since energy is continually transferred from large to small scales where dissipation by heating finally occurs. In order to remove such energy from the model, as well as to prevent the growth of spurious computational aliasing instabilities, a weak background damping term is added to the inviscid model equations (see section 2f). In addition to explicitly resolving processes associated with turbulence, the "quasi-inviscid" equations allow for more direct comparison between

model results and analytical density current theory since the latter is almost exclusively inviscid.

The version of the outflow model used in this study is dry, two-dimensional, slab-symmetric, and Eulerian. Although moisture and precipitation processes are important in creating a storm downdraft and associated outflow, they likely play a minor role in the dynamics of the outflow itself. The major advantage of using a dry model is that the results are not complicated by cloud generation at the gust front, although such processes can be important (e.g., Seitter, 1983) and will be examined in the future using a moist version of the model.

The assumption of two-dimensionality is a good first approximation for density currents (e.g., Huppert, 1982; Britter and Simpson, 1978, 1981; Simpson and Britter, 1980), and therefore should be equally valid for outflows. Note that in two dimensions, the outflow is assumed to be infinitely long, and therefore all environmental air *must* pass up and over the gust front.

Although axisymmetric geometry is probably more physically realistic than slab symmetry for modeling most outflows, the preclusion of ambient wind shear in the former limits such a model to a narrow class of problems. As a result, we utilize slab symmetry in the static-environment experiments presented here to form a basis for future simulations in sheared regimes.

b. Model equations

The outflow model equations are fully prognostic and therefore compressible. Although such a system admits meteorologically unimportant sound waves, its flexibility to changes in numerical schemes, grid structure, and boundary conditions makes it attractive for use in this and future studies. As discussed below, the computational time step limitation imposed by the presence of sound waves is overcome by employing a quasi-compressibility approximation (section 2c).

The prognostic equations for the horizontal velocity v, the vertical velocity w, the potential temperature θ, and the nondimensional *perturbation* pressure π' for a compressible, non-rotating, inviscid, adiabatic fluid in Cartesian coordinates are

$$\frac{\partial v}{\partial t} + \frac{\partial}{\partial y}(vv) + \frac{1}{\bar{\rho}}\frac{\partial}{\partial z}(\bar{\rho}wv) + C_p\bar{\theta}\frac{\partial \pi'}{\partial y} = 0 \qquad (4)$$

$$\frac{\partial w}{\partial t} + \frac{\partial}{\partial y}(vw) + \frac{1}{\bar{\rho}}\frac{\partial}{\partial z}(\bar{\rho}ww) + C_p\bar{\theta}\frac{\partial \pi'}{\partial z} - g\left(\frac{\theta}{\bar{\theta}} - 1\right) = 0 \quad (5)$$

$$\frac{\partial \theta}{\partial t} + v\frac{\partial \theta}{\partial y} + w\frac{\partial \theta}{\partial z} = 0 \qquad (6)$$

$$\frac{\partial \pi'}{\partial t} + \frac{c_s^2}{\bar{\rho}C_p\bar{\theta}^2}\left\{\frac{\partial}{\partial y}(\bar{\rho}\bar{\theta}v) + \frac{\partial}{\partial z}(\bar{\rho}\bar{\theta}w)\right\} = 0 \qquad (7)$$

where C_p is the specific heat of dry air at constant pres-

sure, g is the gravitational acceleration, and π = $(p/p_0)^{R_d/C_p}$ where p_0 is a reference pressure of 1000 mb and R_d is the gas constant for dry air. An overbar denotes basic state variables which are functions only of height z, c_s is a constant speed of sound, and all other variables which are neither primed nor barred represent the sum of the (hydrostatic) basic state and the perturbation. In writing (4)–(7), we have made use of the equation of state $p = \rho R_d T$ where p is the dimensional pressure and ρ is the density. This system of equations (with appropriate moisture equations) has been used successfully for many years to model deep convection in two and three dimensions (e.g., Soong and Ogura, 1973; Klemp and Wilhelmson, 1978; Wilhelmson and Klemp, 1978; Wilhelmson and Chen, 1982; Droegemeier and Wilhelmson, 1985a,b).

The pressure equation (7) is a simplified version of the full form used by Klemp and Wilhelmson (1978):

$$\frac{\partial \pi'}{\partial t} + \frac{\bar{c}^2}{\bar{\rho} C_p \bar{\theta}_v^2}\left\{\frac{\partial}{\partial y}(\bar{\rho}\,\bar{\theta}_v v) + \frac{\partial}{\partial z}(\overline{\rho \theta_v} w)\right\} = f_\pi \qquad (8)$$

where

$$f_\pi = -v\frac{\partial \pi'}{\partial y} - w\frac{\partial \pi'}{\partial z} - \frac{R_d \pi'}{C_v}\left(\frac{\partial v}{\partial y} + \frac{\partial w}{\partial z}\right) + \frac{c^2}{C_p \theta_v^2}\frac{d\theta_v}{dt} \qquad (9)$$

and where θ_v is the virtual potential temperature, C_v is specific heat of dry air at constant volume, and $\bar{c}$ is the adiabatic sound speed which is a function only of height. The terms in f_π are known to have relatively little influence on physical processes in cloud simulations (Klemp and Wilhelmson, 1978), and consequently we set $f_\pi = 0$ in the outflow model. Since the model developed for this study is distinctly different from the Klemp–Wilhelmson cloud model, particularly with respect to the treatment of eddy diffusion, we provide below a complete description of our numerical solution techniques.

c. The quasi-compressibility approximation

The quasi-compressibility approximation (Droegemeier, 1985; Anderson et al., 1985) involves artificially slowing down the sound wave modes in the model so that a larger, more economical time step may be used. This technique is based on work by Chorin (1967), who addressed the opposite problem of inserting artificial sound waves into an incompressible set of equations. We will defer a rigorous examination of the quasi-compressibility approximation to a forthcoming paper and discuss here only its general philosophy and impact on simulated outflows.

Since the gravity and sound wave modes are both functions of the sound wave phase speed in the full set of hydrodynamic equations (e.g., Ogura and Charney, 1962), one must ensure that an artificial reduction in the sound speed will not "significantly" alter the physically important gravitational modes.

To illustrate this point, we linearize the gravity and sound wave terms of (4)–(7) around a vertically-stratified, motionless, hydrostatic basic state. Performing a conventional perturbation analysis yields the frequency equation (see Appendix)

$$\beta\sigma^4 - \sigma^2\left[c_s^2(l^2 + m^2) + g\beta S_\theta + c_s^2\frac{(S_\rho + S_\theta)^2}{4}\right] + c_s^2 l^2 g S_\theta = 0 \qquad (10)$$

where σ is the frequency, l and m are the horizontal and vertical wavenumbers, respectively, β is a tracer associated with the temporal pressure derivative (see Appendix), and

$$S_\theta = d(\ln\bar{\theta})/dz, \quad S_\rho = d(\ln\bar{\rho})/dz.$$

It is clear from (10) that the gravity and sound wave modes are coupled. If we neglect the term $\partial\pi'/\partial t$ in the pressure equation (A5) (i.e., assume that $\beta = 0$), this is equivalent to assuming that $c_s \rightarrow \infty$ (the anelastic approximation). Equation (10) then becomes

$$-\sigma^2\left[(l^2 + m^2) + \frac{(S_\rho + S_\theta)^2}{4}\right] + l^2 g S_\theta = 0, \qquad (11)$$

and thus compressibility effects are assumed to be important only in pressure changes associated with the vertical wind (Anderson et al., 1985).

In our model, called the *quasi-compressible outflow model* or QCOM, we retain the temporal pressure derivative in (7) [see also (A5) in the Appendix], and thus the model equations contain two gravity wave modes and two "pseudo" sound waves which travel at the imposed speed c_s (Anderson et al., 1985). Provided that c_s is "sufficiently" large, we would expect the solution of the quasi-compressible equations to approach that of the anelastic system. If, on the other hand, c_s is close to speed of the fastest signal in the model (i.e., the outflow), then the redistribution of mass will be incorrectly represented due to the artificially strong coupling between the gravitational and acoustic modes.

To quantify this point, it is useful to examine the ratio between the elastic energy E (i.e., the energy associated with the acoustic modes; Eckart, 1960) and the kinetic energy K (here a result of buoyancy forces):

$$\frac{E}{K} = \frac{p'^2/\bar{\rho}c_s^2}{\bar{\rho}(v^2 + w^2)} \qquad (12)$$

where p' is the perturbation pressure. Table 3 shows values for this ratio based on typical parameters in our simulations ($p' = 5$ mb, $\bar{\rho} = 1$ kg m^{-3}, $v = 30$ m s^{-1}, $w = 10$ m s^{-1}) as a function of c_s. For $c_s > 50$ m s^{-1} (approximately twice the fastest velocity in this example), the elastic energy is small compared to the kinetic energy, and the model solution is relatively independent of c_s (see section 2f). If one were interested in detailed energetics of the flow field, careful consideration would be advised before using the quasi-compressible system.

d. Boundary conditions

The lower boundary in the model is a rigid, free-slip plate ($w = 0$ at $z = 0$). In most numerical models, the upper boundary is taken to be a rigid, free-slip plate ($w = 0$ at $z = z_{top}$). However, such a condition is not appropriate for the QCOM for two reasons. First, we often initialize the outflow by prescribing a vertical downflow of cold air at the upper boundary (Droegemeier, 1985). This method of initialization is more easily handled if the upper boundary is not rigid (one could, however, define an orifice at a rigid boundary, e.g., Kao et al., 1978). In addition, we desire to initialize the outflow by prescribing a horizontal influx of cold air into the domain through a lateral boundary. If a rigid upper boundary condition is used in this case, the hydrostatic component of the pressure increases everywhere in the domain (much like blowing air into a closed box; Droegemeier, 1985), thereby causing significant nonphysical alterations in the solution (e.g., strong environmental return flow above the outflow as in Fig. 3b). The easiest way to remove this large pressure buildup is to allow air to pass out through the upper boundary. Consequently, the vertical velocity at the top of the QCOM is *not* set equal to zero. Rather, we define a row of fictitious grid points above the top of the domain which are held fixed at constant pressure, potential temperature, and horizontal velocity. This "constant pressure" upper boundary condition allows the computation of w at the upper boundary (subject to the condition that the vertical flux of w is zero), and also prevents an artificial buildup of pressure in the domain. Note that this type of boundary condition is needed here only when mass is continually being added to the computational domain; such is not the case in standard cloud models, and thus a rigid upper boundary usually suffices (note that although our upper boundary condition radiates sound waves, it is totally reflective for vertically propagating gravity waves).

The lateral boundary conditions are designed to allow internally generated waves to pass freely out of the model domain with minimal reflection and subsequent contamination of the solution. Our formulation is identical to that used by Klemp and Wilhelmson (1978) (see also Klemp and Lilly, 1978), with an intrinsic gravity wave phase speed of 30 m s^{-1} in all experiments.

e. Finite difference equations

The grid system used in the QCOM is the standard Cartesian staggered mesh employed in most cloud models. The thermodynamic variables (θ, π') are located at the center of a grid cell, while the velocity variables (v, w) are positioned at the edges. Although this type of grid produces greater accuracy for the mass variables than an unstaggered mesh, the computational time step is a factor of two more restrictive.

In writing the finite difference equations, we use the standard operator notation given by Lilly (1965):

TABLE 3. Ratio (in percent) of the elastic (E) and kinetic (K) energies as a function of the imposed sound speed c_s for a typical simulated outflow (see the text for details).

c_s (m s^{-1})	E/K (%)
50	10
100	2.5
200	0.6
300	0.3
350	0.2

$$\delta_{n\xi}\phi(\xi) = \frac{\phi(\xi + n\Delta\xi/2) - \phi(\xi - n\Delta\xi/2)}{n\Delta\xi} \quad (13)$$

$$\overline{\phi(\xi)}^{n\xi} = \frac{\phi(\xi + n\Delta\xi/2) + \phi(\xi - n\Delta\xi/2)}{2} \quad (14)$$

where ϕ denotes a dependent variable, ξ is the independent variable, and $n\Delta\xi$ is the interval over which the operation takes place. Applying these operators to the set of governing equations (4)–(7) yields

$$\delta_{2t}v + \delta_y(\overline{v}^y\overline{v}^y) + \delta_z\frac{\overline{(\overline{\rho}^z\,\overline{w}\,\overline{v}^z)}^y}{\overline{\rho}} + C_p\overline{\theta}\delta_y\pi' = 0 \quad (15)$$

$$\delta_{2t}w + \delta_y(\overline{v}^z\overline{w}^y) + \delta_z\frac{\overline{(\overline{\rho}^z\overline{w}^z\,\overline{w}^z)}}{\overline{\rho}^z}$$
$$+ C_p\overline{\theta}^z\,\delta_z\pi' + g\left(\frac{\overline{\theta}^z}{\overline{\theta}^z} - 1\right) = 0 \quad (16)$$

$$\delta_{2t}\theta + \overline{v\delta_y\theta}^y + \overline{\overline{\rho}^z\,w\delta_z\theta}^z\,/\overline{\rho} = 0 \quad (17)$$

$$\delta_{2t}\pi' + \frac{c_s^2}{\overline{\rho}C_p\overline{\theta}^2}[\overline{\rho}\overline{\theta}\delta_y v + \delta_z(w\overline{\rho}^z\,\overline{\theta}^z)] = 0. \quad (18)$$

The time derivatives are evaluated using the second-order leapfrog scheme, and all spatial differences are centered and of second-order accuracy. Although higher order schemes would have provided better accuracy and an improvement in phase errors (particularly for small scale features), the second-order scheme was chosen for its simplicity, particularly near the lateral boundaries. Following Wilhelmson and Chen (1980), the potential temperature equation (17) is written in advective form to provide independence from the pressure equation (18). In addition, $\overline{\rho}$ is included in the vertical derivatives to improve conservation (Chen, 1980).

The computational time step for the QCOM is based on the CFL condition for linear sound waves

$$\Delta t \leq \frac{1}{2c_s}\left\{\frac{1}{(\Delta y)^2} + \frac{1}{(\Delta z)^2}\right\}^{-1/2} \quad (19)$$

where Δy and Δz are the horizontal and vertical grid spacings, respectively, and c_s is the *imposed* sound speed. This equation differs by a factor of ½ from the

one presented by Klemp and Wilhelmson (1978) because our analysis is based on a leapfrog scheme, rather than on a forward-in-time operator for the sound wave terms. For typical parameters of $\Delta y = \Delta z = 100$ m and $c_s = 100$ m s^{-1} (section 4), the linear stability condition is $\Delta t \leqslant 0.35$ s. We use a smaller value of $\Delta t = 0.25$ s to avoid the generation of spurious instabilities by the boundary conditions. This smaller time step is further justified since the value 0.35 s represents the upper limit to *linear* stability, while the equations we are solving are highly nonlinear.

f. Numerical smoothing

Two types of numerical filters are used in the QCOM. The first is the Robert (1966) time filter which removes any tendency for splitting associated with the leapfrog scheme, and also damps physically unimportant high frequency sound waves (Asselin, 1972 and Schlesinger et al., 1983).

The second filter is a spatial background damping term which is added to the right-hand side of each prognostic equation (except for pressure) to discourage the growth of nonlinear (aliasing) instabilities. Lagged in time to maintain computational stability, this term is expressed in finite difference notation as

$$K_y \delta_{yy} \phi^{n-1} + K_z \delta_{zz} \phi^{n-1}$$

This filter is applied only at interior grid points and only to perturbation quantities. Note that K_z is allowed to differ from K_y, even when the grid size is the same in both coordinate directions. Although difficult to justify rigorously, this approach is used because shearing instabilities atop the simulated outflows (similar to the eddies in Fig. 2) are sensitive to the magnitude of the vertical mixing coefficient (Droegemeier and Wilhelmson, 1985c). Excessive vertical computational smoothing completely smears out this shear interface, and thus prohibits the development of instabilities and associated turbulence. This topic is addressed in detail in section 4.

In using a second-order damping term, the QCOM is no longer inviscid. Without some background numerical damping, the model quickly builds up energy in the smallest scales and becomes unstable. It is important to realize that, although this mixing is meant to suppress *computationally induced* modes, it also acts in the model as a crude representation of *eddy viscosity* (with a constant eddy coefficient). The values chosen for the mixing coefficients, however, represent only the minimum amount of smoothing needed to maintain a computationally stable solution.

To justify the absence of a turbulence parameterization in the QCOM, simulations using the "quasi-inviscid" equations (i.e., Eqs. (4) to (7) including the second-order background smoother) were compared with those which also included a Smagorinsky (1963) eddy viscosity parameterization (e.g., Soong and Ogura,

1973). Since Smagorinsky's formulation states that the eddy coefficient K is proportional to Δ where $\Delta = (\Delta y \Delta z)^{1/2}$, the importance of the eddy terms diminishes as the grid resolution is refined (Deardorff, 1975). Our model results indeed verify this fact, and are found to be nearly the same with or without the Smagorinsky parameterization provided that high spatial resolution ($\sim$50 to 100 m for this problem) is used (see also Klaassen and Clark, 1985).

g. Model initialization and integration

All initial model data fields are horizontally uniform and in hydrostatic balance. Data required as input to the model are the vertical profiles of potential temperature and horizontal wind speed, along with the surface pressure. The basic state pressure $\bar{\pi}$ and density $\bar{\rho}$ are computed using

$$\delta_z \bar{\pi} = -\frac{g}{C_p \bar{\theta}^{\bar{z}}} \tag{20}$$

$$\bar{\rho} = \frac{\bar{\pi}^{C_v/R_d} P_0}{\bar{\theta} R_d} \tag{21}$$

The outflow may be initialized in the model by one of several different methods (Droegemeier, 1985). In this paper, we utilize a lateral inflow technique, which involves placing a continuous source of cold air at a lateral boundary. In this case, we do not represent the creation of an outflow by downdraft air; rather, we assume that the outflow is already on the ground, and that it may be represented by a "jet" of cold air moving horizontally.

In creating the outflow, a specified number of temperature grid points in the left-most vertical column (i.e., those located one-half grid interval in from the left lateral boundary) are held fixed in time at a specified temperature colder than ambient. To insure that the flow is purely horizontal at the cold-air source region, the perturbation pressure at the lateral boundary is hydrostatically balanced using

$$\delta_z \pi' = \frac{g}{C_p \bar{\theta}^{\bar{z}}} \left(\frac{\overline{\theta - \bar{\theta}^{\bar{z}}}}{\bar{\theta}} \right), \tag{22}$$

and is also held fixed in time. As the integration begins, the horizontal perturbation pressure gradient across the cold air column "draws" air into the model domain. By varying the magnitude of the cooling, we control the rate at which cold air enters the outflow. All boundary conditions within the cold-air source region are as described in section 2d, with one exception: due to the condition of continuous inflow, a zero horizontal gradient condition on the horizontal velocity replaces the gravity wave radiation condition (i.e., v at the left boundary is set equal to the value computed one grid point to the right). Above the cold-air source region, the radiation condition applies.

It is important to note that initializing an outflow as a column of cold air having a specified height and temperature deficit (or equivalently, inflow velocity) represents an overspecification of the physical problem. For example, for a given temperature deficit, a real outflow may be deeper or shallower than the height imposed in the model. Nevertheless, this technique has been used successfully by Crook and Miller (1985) in a modeling study of undular bores, and is equally appropriate for simulating an outflow which has moved away from its parent downdraft.

h. Evaluation of the quasi-compressibility approximation

In contrast to many other types of numerical models (e.g., terrain models), there exist no simple analytical atmospheric problems against which the outflow model solutions may be compared. Therefore, in order to quantitatively evaluate the performance of the QCOM, we compare its results to those produced by a *fully compressible outflow model* (FCOM) under identical conditions (Droegemeier, 1985). The FCOM shares the same computational framework (e.g., boundary conditions, grid structure, initialization techniques) as the QCOM; however, unlike the QCOM, the FCOM conserves total energy, and is also quite accurate since the momentum equations actually predict momentum rather than velocity (i.e., mass and energy are advected in a consistent manner—see Droegemeier, 1985). The only major limitation associated with the FCOM is the small computational time step required due to the presence of sound waves (time splitting this code would provide only a minor increase in run time). This feature makes the FCOM prohibitively expensive to run as a high resolution production code.

In a series of extensive tests, the QCOM was compared to the FCOM by simulating the evolution of positively and negatively buoyant thermals in quiescent neutral and stratified environments, using both periodic and open boundary conditions. In each set of experiments, one simulation was made with the FCOM (this experiment was regarded as providing the "correct" or control solution), and four other simulations with identical initial and boundary conditions were made with the QCOM using imposed sound speeds of 350, 200, 100 and 50 m s^{-1}.

To summarize the results of these tests, we note that the domain averaged kinetic energy, defined as

$$\langle \mathrm{KE} \rangle = \frac{1}{2} \int \int_A \rho(v^2 + w^2) dy dz, \qquad (23)$$

varies by less than 10% (relative the FCOM) among all of the simulations (Fig. 4), with the exception of the $c_s = 50$ m s^{-1} experiment. In this case, errors in $\langle \mathrm{KE} \rangle$ range from 15 to 45% (the largest values are associated with the stable environment tests), indicating that the sound waves are moving slowly enough to significantly

influence the velocity field i.e., the coupling of the sound and gravity wave modes is strongly evident. Although these *integrated* errors appear somewhat large, we found only minor (for our purposes) quantitative differences among any of the simulated fields. For example, the maximum vertical velocity induced by the gust front, shown in Fig. 5 as a function of time and c_s, showed little variation for $c_s > 50$ m s^{-1} (the discrepancy between the $c_s = 350$ m s^{-1} and the FCOM experiment results from the use of a model-determined, fully variable sound speed in the latter). The corresponding pressure perturbations at the gust front were found to vary by only a few percent for $c_s > 50$ m s^{-1} (see also Anderson et al., 1985). We therefore use $c_s = 100$ m s^{-1} in all experiments to follow.

Based on these and other tests, we conclude that the QCOM is a viable alternative to the more expensive and somewhat more accurate FCOM (timing statistics from many simulations show that, in general, the QCOM runs three to four times faster than the FCOM). For most simulations, it appears that the imposed sound speed in the QCOM should be no less than twice the speed of the fastest-moving physical mode in the model (e.g., the outflow or the fast gravity waves). This rule of thumb should prevent the artificially slow-moving sound waves from significantly interfering with the physical modes of the solution.

It is interesting to note that in tests with the Klemp and Wilhelmson (1978) three-dimensional cloud model, the greatest improvement in model efficiency was obtained by using both a time-splitting procedure and a reduced (constant) sound speed. Comparative experiments for deep convective cloud simulations, including a discussion of alterations in energetics induced by the quasi-compressible assumption, will appear in a forthcoming paper.

3. Outflow sensitivity experiments

In this section we examine outflow morphology and structure by independently varying three fundamental parameters: 1) the vertical shape profile of the imposed temperature deficit, 2) the depth of the cooling region, and 3) the magnitude of the imposed cooling. This approach allows one to span parameter spaces of outflow behavior under widely varying, yet controlled conditions, and therefore isolate specific relationships between two of the outflow variables while holding the third fixed.

In order to simplify interpretation of the model results, all simulations are conducted in a calm, dry adiabatic atmosphere ($\bar{\theta} = 300$ K) without surface friction. Although largely unrealistic, except perhaps in the boundary layer, these conditions allow for clear interpretation of the model results without the complicating effects of gravity waves and ambient wind shear. Furthermore, such an environment provides for more direct comparison of model results with laboratory den-
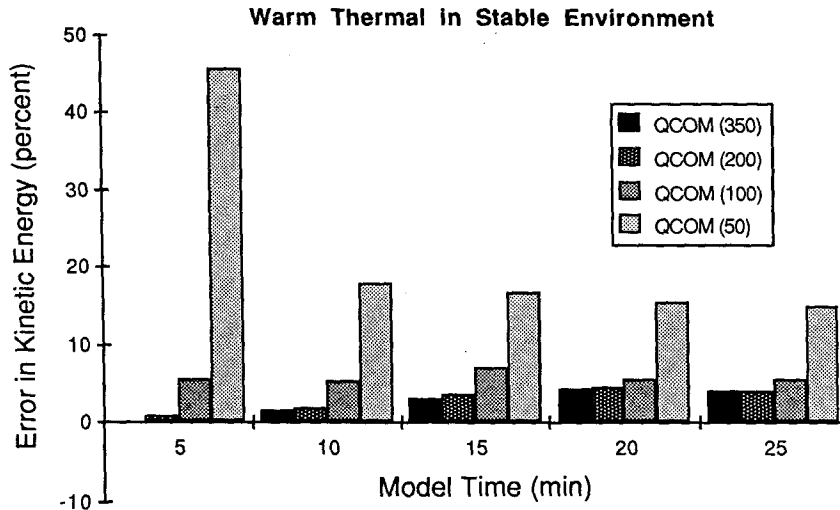
Warm Thermal in Stable Environment

FIG. 4. Error in kinetic energy (percent, relative to the Fully Compressible Outflow Model) for simulations of a warm thermal in a stable environment ($d\bar{\theta}/dz = 4$ K km^{-1}) using several imposed sound wave phase speeds (m s^{-1}, shown in parentheses) in the Quasi-Compressible Outflow Model (QCOM).

sity current experiments since constant potential temperature with height in a compressible atmosphere is equivalent to constant density in an incompressible fluid (Simpson and Britter, 1980). Simulations using more realistic environmental conditions are discussed in Part II of this paper.

Because of the large number of simulations conducted during the course of these experiments (only a few of which are discussed herein), a relatively coarse, uniform grid mesh of 200 m is used (higher resolution simulations are discussed in section 4 and Part II). The

computational mixing coefficients for all experiments in this section are $K_y = 300$ m^2 s^{-1} and $K_z = 75$ m^2 s^{-1}, with a time step of 0.5 s. Each simulation is curtailed when the propagating gust front nears the lateral boundary.

a. Temperature profile experiments

To address the influence of the vertical temperature deficit profile in the cold air column to modeled outflow behavior, we compare simulations using the three

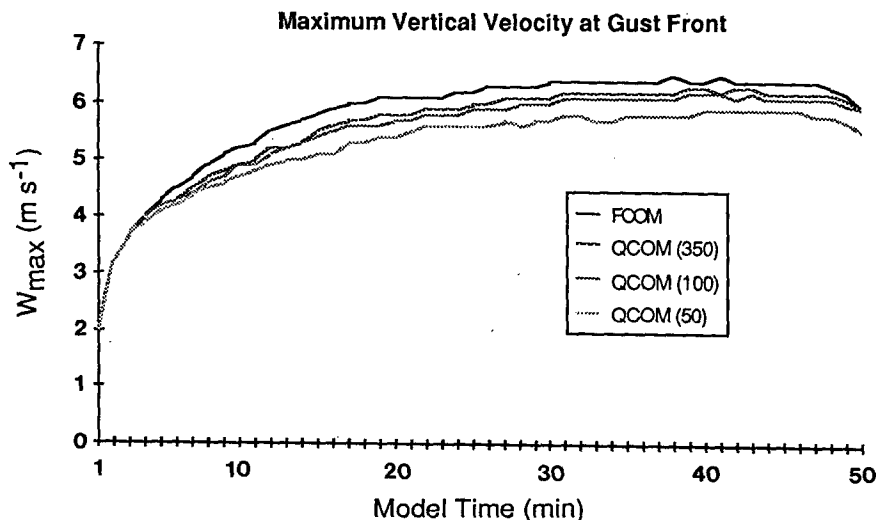**Maximum Vertical Velocity at Gust Front**

FIG. 5. Time series plots of the maximum vertical velocity induced at the gust front for the fully compressible outflow model (FCOM), and for imposed sound speeds of 350, 100 and 50 m s^{-1} in the quasi-compressible outflow model (QCOM).

vertical shape profiles in Fig. 6: a step function, a linear profile, and a cosine squared profile defined by:

$$\Delta\theta = \Delta\theta_0 \cos^2\left(\frac{\pi}{2}\beta\right) \quad \text{for} \quad \beta \le 1,$$

$$\beta = \frac{z - z_c}{z_r} \tag{24}$$

where $\Delta\theta_0$ is the magnitude of the imposed potential temperature perturbation, and z_c and z_r are the height of the perturbation center above the ground and its vertical radius, respectively. The model domain in these simulations is 40 km long and 8 km tall.

Apart from the desire to examine outflow characteristics for different shapes of the cooling region, justification for using the profiles in Fig. 6 is based on internal outflow temperature measurements reported by Goff (1975; see his cases E and F).

We impose the constraint in these simulations that the *vertically integrated* temperature perturbation within the cold air column be the same for each of the three temperature profiles (e.g., -2 K for each profile in Fig. 6). This implies that the surface hydrostatic perturbation pressure in the cold air column is also the same. Since outflows are driven primarily by the hydrostatic pressure excess in the cold outflow air, this constraint is necessary in order to make direct comparisons among the simulations.

Figure 7 shows contour plots of the perturbation potential temperature field (dashed contours) at 40 min for the three varied profile simulations (only the lower portions of the domains are pictured). Stippled regions enclose positive vertical velocities (upward motion) greater than 6 m s^{-1} and cross-hatched regions denote downward motion stronger than -3 m s^{-1}. In each case the outflow has reached a quasi-steady configuration (due to the free-slip lower boundary, however, the outflow continually accelerates), and exhibits the characteristic shape depicted schematically in Fig. 1. Note the "overturning wave" located immediately behind each outflow head. This feature is a direct consequence of the strong solenoidally-induced circulation

within the outflow head (Fig. 1 and Mitchell and Hovermale, 1977), and has been observed in the atmosphere (Wakimoto, 1982) and studied analytically in two dimensions by Stern and Pratt (1985) for a piecewise-uniform vorticity flow.

The most obvious difference among the simulations in Fig. 7 is that the outflow head in the step profile run (Fig. 7a) is nearly twice as deep as in the other two cases. This result may be explained by noting that horizontal vorticity is generated in these outflows by horizontal temperature gradients, i.e.,

$$\partial\xi/\partial t \sim \partial\theta'/\partial y \tag{25}$$

where ξ is the horizontal vorticity $\partial w/\partial y - \partial v/\partial z$, and θ' is the perturbation potential temperature. From $z = 1$ to 2 km (middle to top of the outflow), the horizontal difference in θ' across the cold air interface in the step profile outflow is a uniform -2 K, while in both of the other cases it decreases from -2 K at $z = 1$ km to 0 K at $z = 2$ km. As a result, horizontal vorticity from $z = 1$ to 2 km is strongest in the step case, thereby creating a more vigorous circulation and a correspondingly deeper outflow head.

It is important to point out that *below $z = 1$ km,* the vorticity generated via Eq. (25) is *smaller* for the step profile case ($\Delta\theta'$ across the front $= -2$ K uniformly from $z = 0$ to 1 km) and *larger* for the other two runs ($\Delta\theta'$ across the front varies from -4 K at $z = 0$ km to -2 K at $z = 1$ km). Thus, even though the *maximum* horizontal vorticity in the step profile simulation ($\sim 1.8 \times 10^{-2}$ s^{-1}) is *smaller* than in the other two cases ($\sim 2.9 \times 10^{-2}$ s^{-1}), its head is still the deepest.

Another interesting observation from Fig. 7 is that the outflow in the linear temperature profile experiment moves the fastest, followed by the cosine profile and then the step function outflow. Based on Eq. (2) alone, this result is somewhat paradoxical since the gust front speed is supposed to be a function of the cold air depth, i.e., one would expect the step function outflow to move the fastest rather than the slowest!

The explanation for this paradox is two-fold, and lies in the internal dynamics of the outflow head. First of all, as described above, the baroclinic generation of horizontal vorticity near the ground is largest in the linear profile simulation, and the associated strong, low-level winds thereby aid the gust front's propagation. In addition, as low-level air is advected from near the ground to the top of the outflow head by the internal solenoidal circulation, a net cooling occurs in the vertical column behind the gust front, accompanied by an increase in the surface hydrostatic pressure (since the temperature is uniform in the step case, no such increase occurs). Therefore, as indicated by Eq. (3) and discussed by Crook and Miller (1985), an outflow with a linear temperature deficit profile will propagate faster than one having a uniform temperature distribution with height, despite the fact that the head is deeper in the latter case.
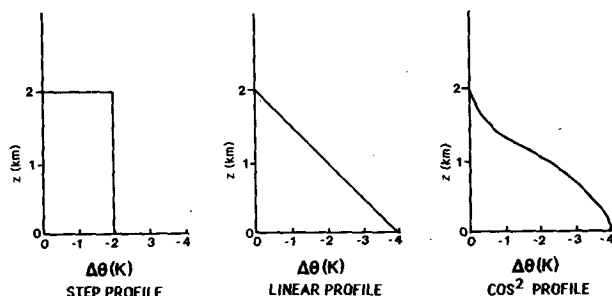

FIG. 6. A schematic representation of the temperature profiles used in the variable shape profile simulations. In each case, the vertically-averaged perturbation potential temperature is -2 K.
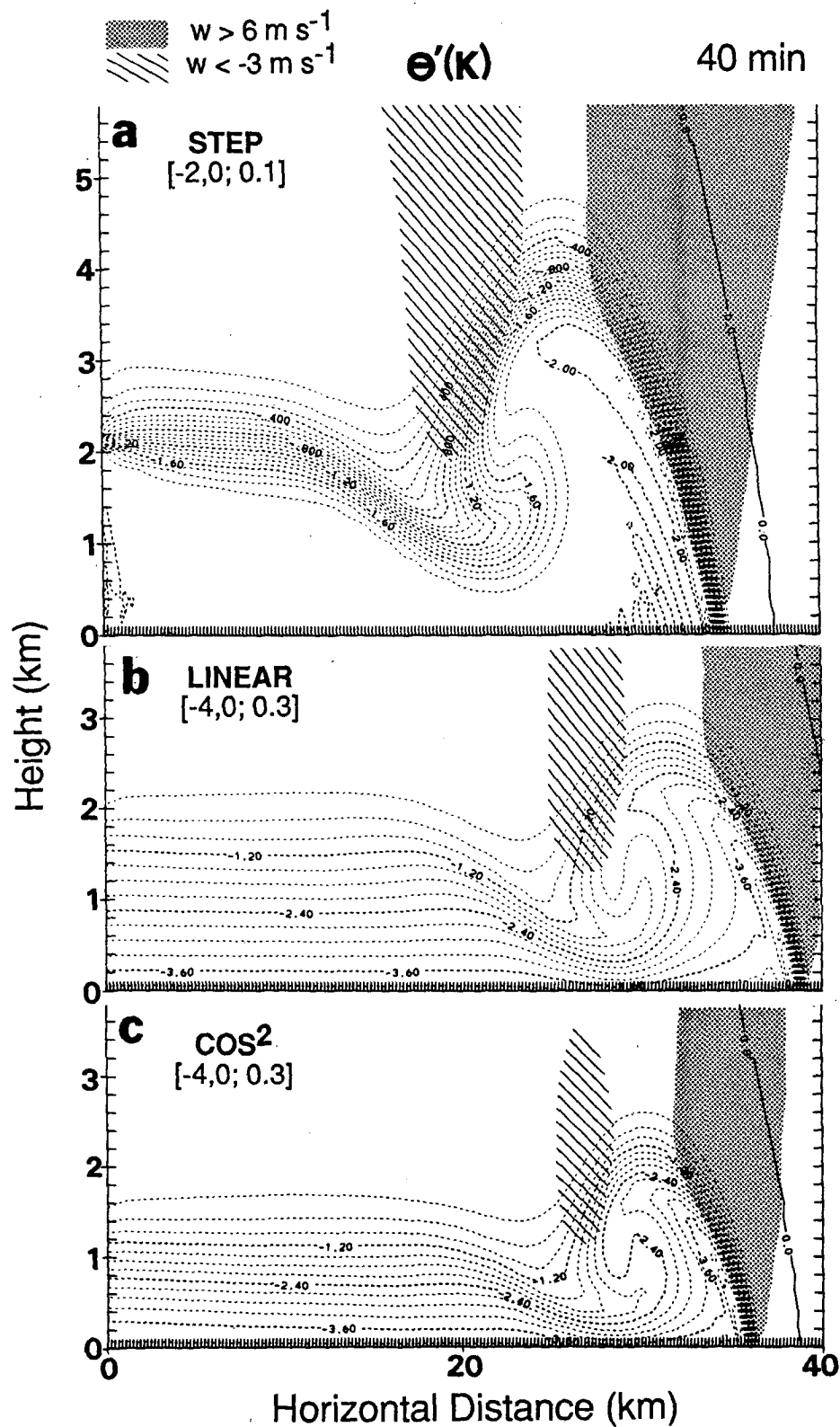
FIG. 7. Vertical cross sections at 40 min of the perturbation potential temperature (deg K) for the variable shape profile simulations. For this and all subsequent figures, the square brackets indicate [minimum value, maximum value; contour interval]. Stippling encloses regions of $w > 6$ m s^{-1} and cross-hatching encloses regions of $w < -3$ m s^{-1}.

It is interesting that even though the step function outflow propagates slower than the other two, and also has weaker maximum surface divergence (-9×10^{-3} s^{-1} compared to -1.3×10^{-2} s^{-1} for the linear and cosine squared profiles), the maximum lifting induced by its gust front is the strongest of all three simulations ($w = 8.1$ m s^{-1} compared to 7 m s^{-1} for the other two cases). Consequently, a fast frontal propagation speed does not necessarily imply large surface convergence or strong frontal lifting (Thorpe et al., 1980).

Figure 8a depicts an important feature which has been noted in previous observational and modeling studies—namely, that a pressure ridge *precedes* the passage of the gust front. The fact that the ridge occurs in advance of the temperature drop indicates that it cannot be hydrostatically induced. Wakimoto (1982) attributes the pressure ridge to the collision of the cold outflow air with the warmer ambient air, i.e., the ridge is dynamically induced. This is consistent with our model results, as documented in Fig. 8b by the horizontal divergence (units of 10^{-4} s^{-1}) and the axis of the pressure ridge (bold dashed line) for the linear profile simulation. It is clear from this figure that the pressure ridge is located in the center of the surface convergence zone (which lies across and slightly ahead of the frontal zone), implying that the ridge is dynamically induced.

b. Temperature magnitude experiments

In this section we examine the sensitivity of modeled outflow characteristics to the magnitude of the imposed temperature deficit. In all experiments the cold air source region is 1 km deep at the lateral boundary, and has a linear temperature deficit profile with height (this profile was chosen based on the structure of many observed and modeled outflows, e.g., Goff, 1975; Klingle, 1985; Crook and Miller, 1985; Droegemeier and Wilhelmson, 1985a). The model domain is 60 km long and 10 km high with a 200 m grid spacing, and the vertically averaged outflow temperature deficits for the six simulations discussed are -0.5, -1.0, -2.0, -3.0, -4.0 and -5.0 K.

Figure 9 shows several computed gust front parameters as functions of the average outflow temperature deficit. The nearly linear relationship between the square of the gust front velocity and the average outflow temperature deficit agrees quite well with both inviscid theory (Eq. 2) and with observed density currents (e.g., Simpson, 1969). The linearity between the maximum surface pressure behind the gust front and the outflow temperature deficit is due to the hydrostatic relation between these two variables. Figure 9 also indicates that both the maximum lifting induced by the gust front and the maximum surface convergence increase substantially for colder outflows. One might therefore be tempted to conclude that colder, faster moving outflows are more likely than relatively warmer outflows

to trigger deep convection. However, one must consider that updrafts along fast-moving gust fronts are susceptible to strong horizontal shear which is sometimes capable of suppressing deep convective development (e.g., Seitter, 1983). Furthermore, the generation of convection at gust fronts depends upon the residence time of air parcels in the condensed state, as well as the depth of the mixed layer and the ambient wind shear (e.g., Droegemeier and Wilhelmson, 1985b).

The increase of maximum vorticity in Fig. 9 with increasing temperature deficit concurs with solenoidal theory (Mitchell and Hovermale, 1977), and also explains the minor variation in head depth for these experiments, i.e., the vorticity and gust front propagation speed increase proportionally with increasing temperature deficit, and together maintain a constant head depth. This agrees with laboratory results of Schmidt (1911) and Simpson and Britter (1980), who showed that the head depth of a density current is typically twice the depth of the following flow upstream.

To gain further insight into the dynamics of these outflows, we compare Froude numbers computed three ways using the observed gust front speeds V_{obs} (Table 4). In the first two methods, we use Eq. (2) with V replaced by V_{obs} and H representing either the average depth of the outflow well behind the head (H_{body}), or the average head depth H_{head}. In the third method, we compute k using Eq. (3).

Table 4 shows that the Froude numbers computed using H_{body} and Seitter's method are quite similar (a result also noted by Koch, 1984). In addition, they are close to the value $\sqrt{2}$ predicted by inviscid density current theory. In contrast, the values of k computed using H_{head} are much smaller, and are in closer agreement with the values 1.1 to 1.2 given by Benjamin (1968) (with H representing the "densimetric mean level of the disturbed interface" in the laboratory density current) and Keulegan (1958) and the value 1.25 obtained by Charba (1974) (with H representing an estimated mean outflow depth). It is interesting that all values of k in this table lie well above the average of 0.77 reported by Wakimoto (1982) for squall line gust fronts. This may be a result of the depth constraint imposed at the inflow boundary (i.e., the Froude numbers greater than unity are a result of forcing the outflows to be artificially shallow for their particular temperature deficits), as well as the absence of surface friction in the outflow model.

The final point to be addressed in this section is the structure of the outflow perturbation pressure field. Figure 10 shows contour plots of (i) the perturbation pressure P (mb), (ii) the perturbation horizontal velocity v (m s^{-1}), and (iii) the vertical velocity w (m s^{-1}) at 40 min for the simulation having a mean outflow temperature deficit of -4 K. The bold solid line in each figure panel denotes the outflow boundary (-0.1 K perturbation isentrope). Figure 10a indicates that the pressure in the body of the outflow (left portion of the figure) is in hydrostatic balance with the temperature
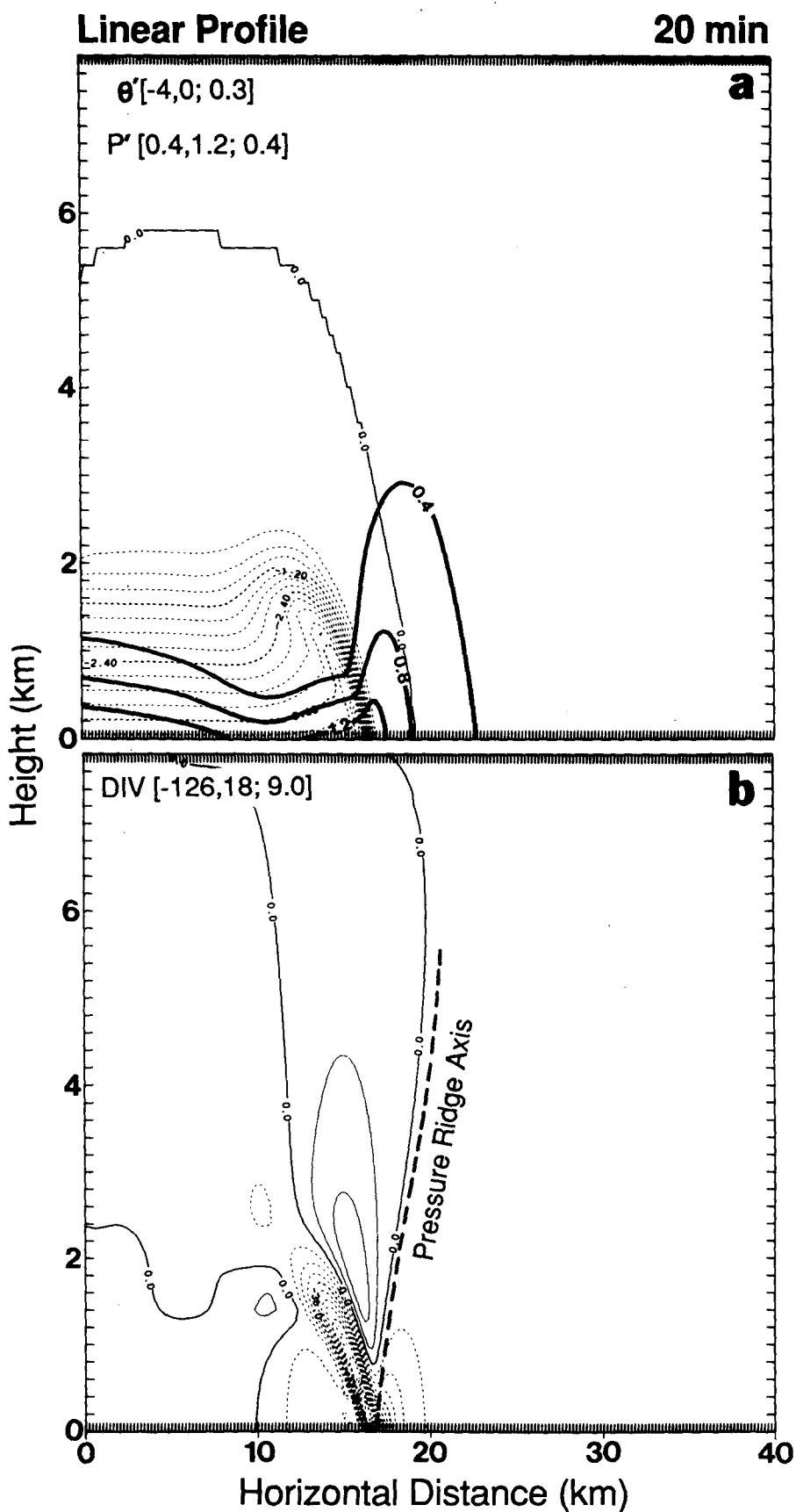
FIG. 8. Contour plots at 20 min in the linear profile simulation of (a) the perturbation potential temperature (deg K, dashed contours) and pressure (mb, solid contours), and (b) the horizontal divergence (units of 10^{-4} s^{-1}) and the axis of the pressure ridge.
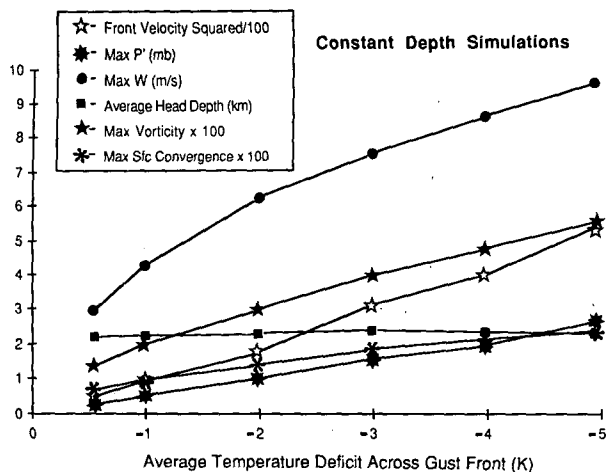
FIG. 9. Several parameters for the constant depth–variable temperature deficit simulations. Units for the horizontal vorticity and divergence are s^{-1}.

field (not shown). Immediately behind the outflow head, however, there exists a large region of negative perturbation pressure (minimum value of −1.8 mb, indicated by the bold L) which extends well down into the cold-air pool. This negative pressure anomaly is associated with the horizontally-oriented circulation set up by the advancing gust front, i.e., the low is cyclostrophically balanced with the model wind field (Figs. 10b and 10c).

We quantify this observation by examining the cyclostrophic wind law in natural coordinates (Holton, 1979):

$$-\frac{1}{\rho}\left(\frac{\partial P}{\partial n}\right) = \frac{V^2}{R_s} \qquad (26)$$

where V is the air velocity in the direction of s, R_s is the radius of curvature, and n is the direction normal to the streamline (taken to be positive when oriented to the left of the flow direction). As discussed by Yau (1979), (26) states that a low pressure area is located to the left (right) of the direction of motion for counterclockwise (clockwise) rotation.

For the example shown in Fig. 10, we take $V \sim 6$ m s^{-1} and $R_s = 1000$ m in the vertical direction from the center of the low, along with the observed pressure gradient to yield

$$\frac{V^2}{R_s} = 0.036 \text{ m s}^{-2}$$

$$\frac{1}{\rho}\left(\frac{\partial P}{\partial n}\right) = 0.040 \text{ m s}^{-2}.$$

Although these values represent only an estimate of the true pressure balance shown in Fig. 10a (i.e., there is a small positive hydrostatic contribution since the low center is located just inside the outflow head), they do suggest that the low pressure is cyclostrophically balanced. Furthermore, we note that the maximum pressure deficit varies nearly linearly from −0.2 mb in the −0.5 K simulation to −2.4 mb in the −5 K case.
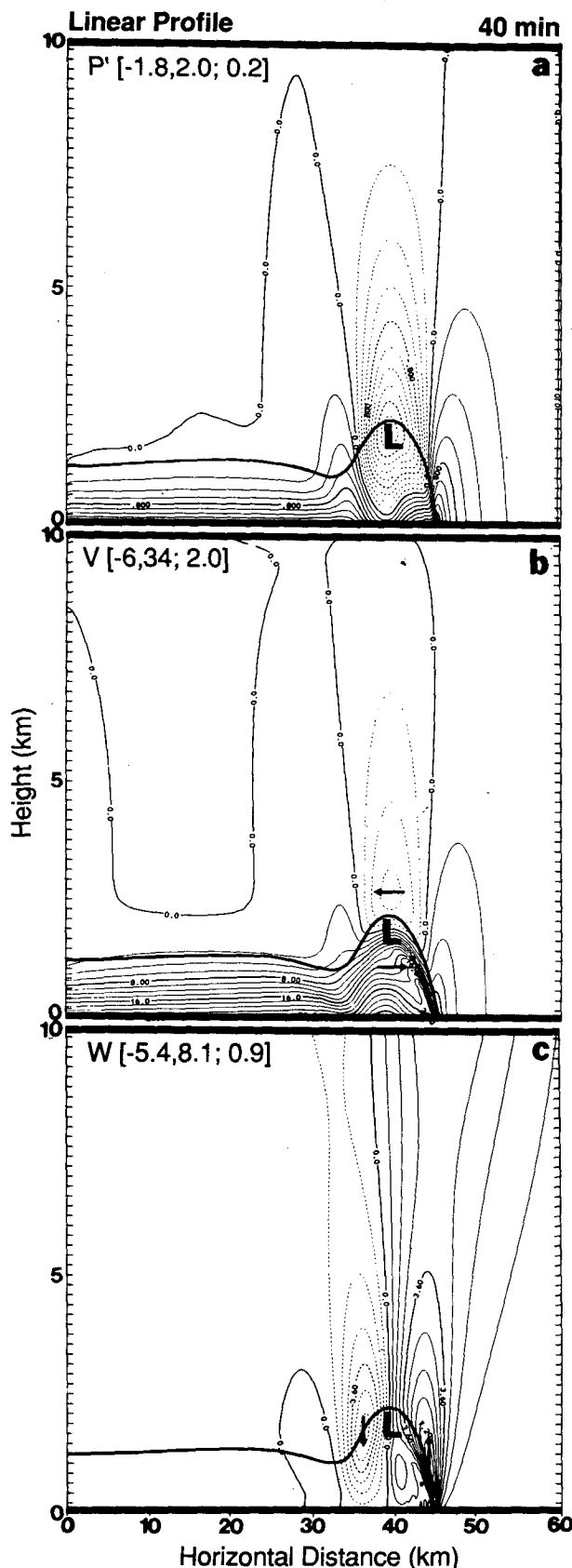
The horizontal pressure gradient at the ground, set up by the rotational pressure deficit aloft, causes air within the body of the outflow to accelerate horizontally as it nears the head. This is illustrated in Fig. 10b, which shows that the maximum horizontal winds are located at the ground directly beneath the low pressure center aloft. As air continues to move toward the gust front, it is decelerated by this same pressure gradient and is also deflected upward by the solenoidal circulation within the outflow head. This finding is consistent with observational studies which show that the surface pressure sometimes decreases after the initial gust front passage (Wakimoto, 1982 Fig. 26; Charba, 1974, Fig. 8), and that a secondary horizontal wind speed maximum is often found well behind the gust front (Wakimoto, 1982, Fig. 26; Charba, 1974, Figs. 4, 8 and 11).

c. Variable outflow depth experiments

The final experiments to be discussed in this section involve systematically varying the depth of the outflow at the left lateral boundary while keeping the imposed temperature deficit constant. To accommodate the wide range of prescribed outflow depths in these simulations, the model domain is 80 km long and 12 km

TABLE 4. Values of the internal densimetric Froude number k computed three different ways for the variable temperature experiments.

Mean outflow temperature deficit	H (m)		ΔP (mb)	V_{obs} (m s^{-1})	k		
	Body	Head			(H_{body})	(H_{head})	(ΔP)
−0.5	1300	2200	0.24	6.9	1.5	1.2	1.5
−1.0	1300	2250	0.50	9.6	1.5	1.1	1.5
−2.0	1300	2300	1.00	13.3	1.4	1.1	1.4
−3.0	1300	2400	1.60	17.7	1.6	1.2	1.5
−4.0	1300	2350	2.00	20.1	1.5	1.1	1.5
−5.0	1300	2300	2.70	23.4	1.6	1.2	1.5
				mean	1.5	1.2	1.5

FIG. 10. Contour plots at 40 min in the Linear Profile simulation of (a) the perturbation pressure (mb), (b) the horizontal velocity (m s⁻¹), and (c) the vertical velocity (m s⁻¹). The bold solid line denotes the outflow boundary (−0.1 K perturbation isentrope), and the L indicates the region of lowest pressure. The arrows in panels b and c depict the general flow (ground-relative) around the low center.

tall. Each outflow temperature deficit has a linear profile with height, and a vertically averaged value of −2 K. Five simulations with imposed outflow depths of 0.5, 1.0, 2.0, 3.0 and 4.0 km corresponding to surface pressure excesses of 0.36, 0.72, 1.44, 2.16 and 2.87 mb, respectively, are discussed.

Table 5 shows the internal densimetric Froude number k computed five different ways for these simulations. The most common method for determining k (method C) involves using the head height H_h and the average potential temperature difference $\overline{\Delta\theta}$ between the outflow and the environment (Wakimoto, 1982). Using this method, k is found to vary from 1.08 to 1.27, all values being less than the theoretical $\sqrt{2}$ yet much larger than those reported for atmospheric density currents (Table 2). It is difficult to determine from Table 5 which method for computing the Froude number is most appropriate. The value $\sqrt{2}$ obtained from inviscid theory must be viewed with some caution since it is based on the premise that all flow within the density current is uniform and traveling at the frontal speed. Despite the large variation in k among the five methods A–E in Table 5, there is a remarkable consistency within each category over the wide range of outflow depths used. Once again, this observation points to a balance between the negative buoyancy in the outflow and its propagation speed, and also reinforces the notion that k is truly a constant of the flow.

Figure 11 shows that the gust front speed and frontal-induced lifting in these experiments are larger for deeper outflows. In contrast, the average surface divergence is nearly a constant (−140 × 10⁻⁴ s⁻¹), independent of the outflow depth. This suggests, as did the results of the previous section, that the magnitude of the gust front-induced convergence is not a simple function of the gust front speed or frontal-relative flow.

The horizontal vorticity within the outflow head in these experiments attains a nearly constant value of 360 × 10⁻⁴ s⁻¹ for outflow depths ≥2 km. Since the outflow temperature deficit is the same in each of these experiments, this observation is consistent with Eq. (25). Note from Fig. 11 that shallower outflows exhibit somewhat smaller values of vorticity at the gust front. This appears to be related to the fact that shallower flows experience a greater retarding influence by the lower boundary condition ($w = 0$) to overturning within the outflow head.

4. Turbulence dynamics

As discussed in section 2 (see Fig. 2), one of the most prominent features in laboratory density currents is

TABLE 5. Values of the internal densimetric Froude number (k) computed five different ways for the variable outflow depth experiments.

Imposed outflow depth (km)	k				
	A	B	C	D	E
0.5	1.2	0.8	1.1	0.8	1.5
1.0	1.4	1.0	1.2	0.8	1.5
2.0	1.5	1.1	1.2	0.9	1.5
3.0	1.4	1.0	1.2	0.8	1.4
4.0	1.5	1.0	1.3	0.9	1.5
Mean	1.4	1.0	1.2	0.8	1.5

A: $H_B, \overline{\Delta\theta}$ ⎫
B: $H_B, \Delta\theta_{max}$ ⎪
C: $H_h, \overline{\Delta\theta}$ (standard method) ⎬ [Eq. (2)]
D: $H_h, \Delta\theta_{max}$ ⎪
E: Seitter's method [Eq. (3)] ⎭
H_B mean outflow body depth
H_h mean outflow head depth
$\overline{\Delta\theta}$ average potential temperature difference across the front
$\Delta\theta_{max}$ maximum potential temperature difference across the front

the growth, mutual interaction, and eventual decay of Kelvin–Helmholtz (KH) shearing eddies. Although these turbulent billows apparently exist in seabreezes (e.g., Simpson et al., 1977), in cold fronts (Young and Johnson, 1984), and in nocturnal drainage wind events (Blumen, 1984), they have never been documented in outflows simulated despite the fact that KH instability is believed to be a major cause of turbulence in such events (e.g., Simpson, 1982). We show in this section that with adequate spatial resolution and proper numerical smoothing, our model is able to resolve turbulent KH eddies atop the outflow, and that these eddies are qualitatively and quantitatively similar to structures found in laboratory density currents.

a. Control simulation

To illustrate the basic features of turbulence in modeled outflows, we first examine a control simulation in which the outflow is initialized as a 2 km high column of cold air having a uniform temperature deficit of -6 K. The model domain is 30 km long and 10 km tall with a 100 m uniform grid. As discussed below, this doubling of the grid resolution relative to previously discussed experiments is necessary for capturing the evolution of turbulence in the simulated flow field (the smaller physical domain size relative to experiments in section 3 was dictated by computer memory limitations). The ambient environment is calm and dry adiabatic with $\bar{\theta} = 300$ K, and the numerical damping coefficients are $K_y = 100$ m^2 s^{-1} and $K_z = 10$ m^2 s^{-1}.

Figure 12 shows contour plots of the perturbation potential temperature, pressure, horizontal and vertical velocity at 20 min for the control simulation. A series

of well-developed KH billows is present at the top of the outflow (Fig. 12a), and a time sequence of data reveals that these eddies form periodically at the outflow head, and then propagate toward the left (relative to the gust front) with time. Associated with each breaking wave is a cyclostrophically balanced pressure minimum (Fig. 12b), in agreement with the results of section 3. Similar periodic pulsations in the surface pressure, detected during the passage of a seabreeze front (Donn et al., 1956), are believed by Simpson and Britter (1980) to be signals of KH instability in the flow above.

The horizontal velocity field (Fig. 12c) is characterized by extremely sharp vertical gradients, particularly near the top of the cold-air pool. The Richardson number (Ri) in this region is ~ 0.2, which is consistent with the necessary (but not sufficient) condition of Ri < 0.25 for the onset of KH instability in a vortex sheet of infinitesimal thickness (e.g., Chandrasekhar, 1961). The vertical velocity field (Fig. 12d) shows that an updraft–downdraft couplet attends each KH billow (at the center of each couplet is a local maximum in horizontal vorticity, with typical values of $\sim 8 \times 10^{-2}$ s^{-1}). Such a velocity pattern may be responsible for low-level, horizontally-oriented roll clouds which are often observed during and after gust front passage. Note that an aircraft flying through the velocity fields in Figs. 12c and 12d would likely encounter significant turbulence due to the large vertical and horizontal shears.

To quantify the similarity between our model results and laboratory density currents, we compute the ratio between the maximum amplitude and the horizontal wavelength of the billows. Our ratios of 0.5 to 0.7 agree quite well with estimates of 0.8 ± 0.1 given by Simpson and Britter (1979). From linear theory of KH instability, the horizontal wavelength of the fastest growing perturbation in a shear layer of thickness h ranges from
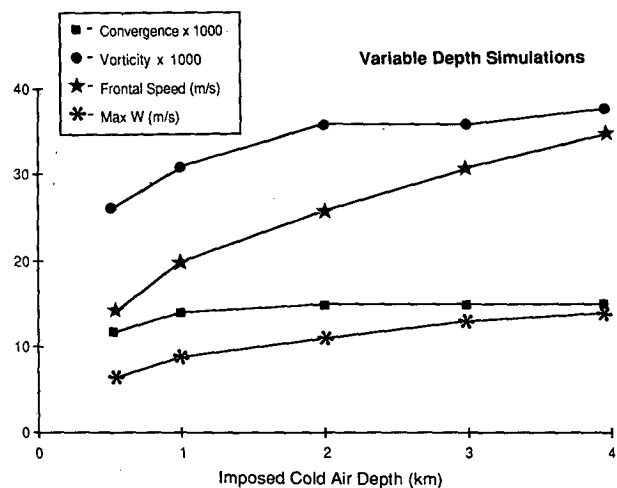

FIG. 11. As in Fig. 9 but for the variable depth–constant temperature deficit simulations.

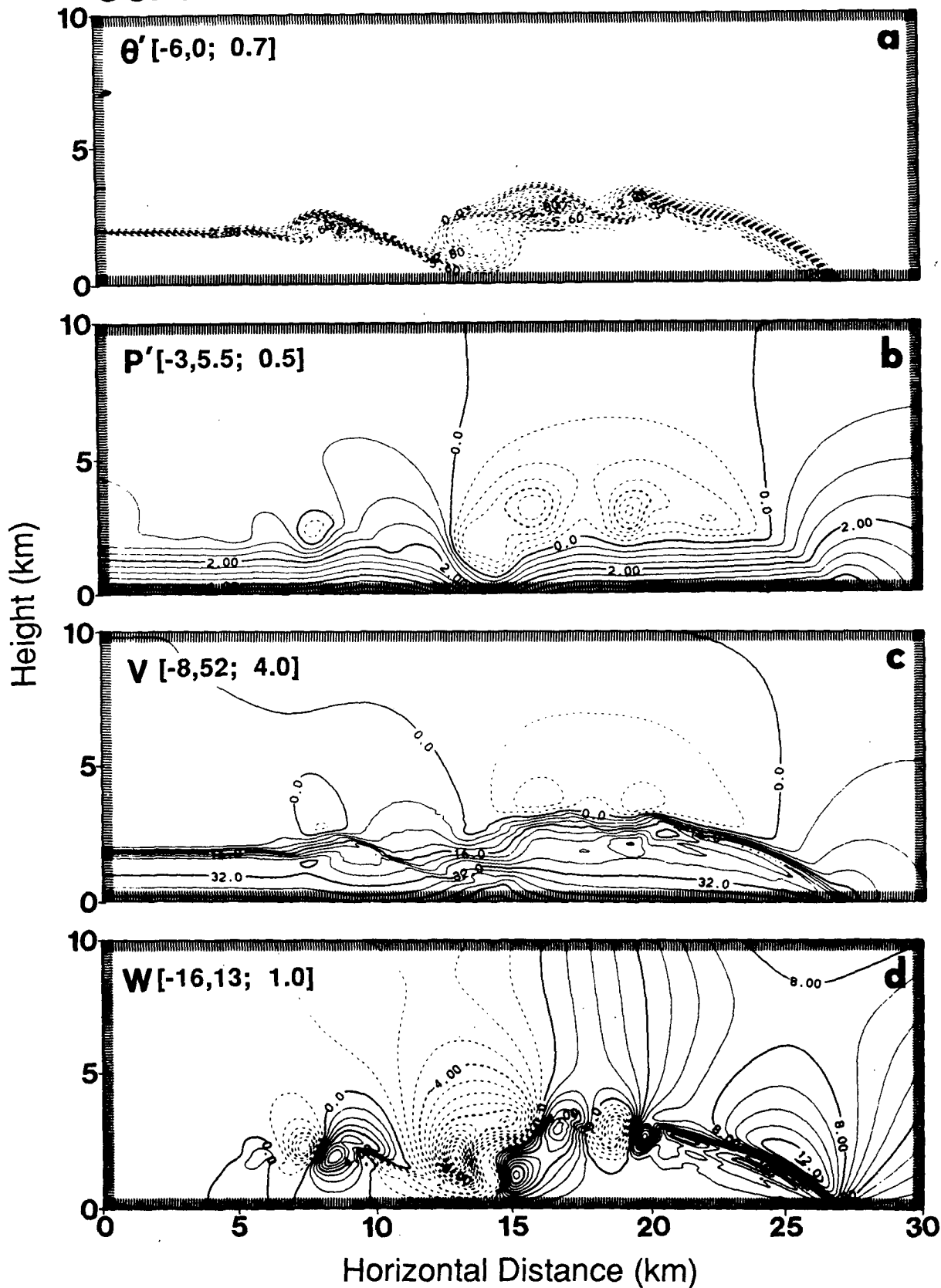# Control Simulation   20 min

θ′ [-6,0; 0.7]   **a**

P′ [-3,5.5; 0.5]   **b**

V [-8,52; 4.0]   **c**

W [-16,13; 1.0]   **d**

Horizontal Distance (km)

Height (km)

FIG. 12. Contour plots at 20 min in the control simulation of (a) perturbation potential temperature (deg K), (b) perturbation pressure (mb), (c) horizontal velocity (m s^{-1}), and (d) vertical velocity (m s^{-1}). Dashed contours represent negative values in all panels.

4.4h (Drazin, 1958) to 7.5h (Miles and Howard, 1964), depending upon the velocity and density profiles across the layer. Although difficult to measure objectively, h in the control simulation is ~500 m, giving a wavelength of 2.2 to 3.8 km for the fastest growing mode. This agrees with the wavelengths shown in Fig. 12, and lends support to the notion that these vortex rolls do indeed result from KH instability.

As a final test to establish similarity between the modeled and laboratory flows, we compute the non-dimensional growth rate G of the billows

$$G = \frac{1}{\Delta u} \frac{d\alpha}{dt} \qquad (27)$$

where Δu is the characteristic velocity difference across the shear layer, and α is the width of the billow normal to the locus of the billow center (Britter and Simpson, 1978). This quantity is also difficult to compute in the simulations due to the mutual interaction among the billows and the continual evolution of the shear layer. Nevertheless, we estimate the billow growth rate to be 0.18 ± 0.06, which is similar to the values 0.25 ± 0.05 obtained in laboratory experiments by Britter and Simpson (1978), and agrees closely with the value of 0.19 given by Brown and Roshko (1974) for a homogeneous shear layer.

Although our numerical model is able to explicitly represent the quasi-two-dimensional growth and interaction of the various KH billows, it is well known that energy cascades and turbulence are incorrectly represented in two-dimensional models (e.g., Deardorff, 1975). This limitation, coupled with the absence of lateral vortex stretching in our two-dimensional model, explains why the simulated KH billows in Fig. 12 never break down into small-scale turbulence (compare Fig. 2).

b. Air parcel trajectories

To further document the kinematic structure of the modeled outflows, we utilize time-dependent air parcel trajectories. Attention is focused primarily on the internal outflow circulation, on identifying the source regions for air composing the KH billows, and on the nature of flow over the gust front. This latter aspect is particularly relevant to the topic of cloud generation by advancing outflows (e.g., Foote, 1984; Droegemeier and Wilhelmson, 1985a,b).

The time-dependent trajectories presented here are computed interactively from model history data, and are based only on the wind field. In computing a trajectory, we specify the time and starting location of the air parcel, along with an extrapolation distance E (which is some small fraction of the total trajectory length, e.g., 100 m). The two-dimensional wind field V_2 is then interpolated to the parcel's location, and the parcel is moved a distance E in time E/V_2. The wind field is then interpolated in space and time to the parcel's new location, and the computations repeat until the parcel reaches one of the model boundaries or until the history data are exhausted.

Due to the transient nature of the outflows in these experiments, we conducted numerous tests to determine the sensitivity of a trajectory path to the parcel's initial starting location, as well as to the time interval of the history data and the specified extrapolation distance. In general, small changes (~2 grid lengths) in the starting location produced only minor variations in the resulting trajectory. Calculations made using history data saved at 30 s intervals were, in most cases, virtually identical to those made using an interval of up to 2 min. Trajectories computed using extrapolation distances of 25, 50, 75 and 100 m were also found to be in general agreement, except in locations where the outflow structure changed rapidly in time (e.g., the KH billows). Based on these tests, we chose to use a 50 m extrapolation distance and 1 min history data interval for the trajectories shown here.

The outflow used for the trajectory analysis is identical to the control case in the previous section, except that the temperature deficit is now linear with height (θ' varies from −6 K at $z = 0$ km to 0 K at $z = 2$ km) and the domain width is increased to 40 km. Despite these changes, the outflow evolution is qualitatively similar to that of the control experiment.

1) INTERNAL FLOW STRUCTURE

Because of the continual formation and mutual interaction of the KH billows in this simulation, the outflow never reaches a truly steady configuration. Consequently, it is difficult to display time-dependent trajectories in a single figure. We therefore present in Fig. 13 a complete history of seven air parcel trajectories superimposed on the perturbation potential temperature field (dashed contours). Labeled A through G, the parcels are placed 200 m apart in a vertical stack beginning at $z = 50$ m, and are released at the left lateral (inflow) boundary 10 min into the simulation. Although the results shown here are for specific air parcels, they are felt to be representative of the motions of other parcels in the regions described.

In the first 5 min after parcel implantation (Figs. 13a, b), the trajectories begin to reveal the vertical structure of the horizontal flow field. Parcels A and B near the ground move the fastest, while parcel G lags behind due to the influence of the developing KH billow atop the cold pool. Note how the parcels in the lower portion of the outflow are catching up with the advancing gust front.

From 17 to 21 min (Figs. 13c, d), parcels F and G become entrained within the large billow at the top of the outflow, while D and E are swept toward the ground by subsidence on the back (left) side of the largest eddy. Parcels A, B and C have entered the outflow head region, and are beginning to rise under the influence of the solenoidal circulation.
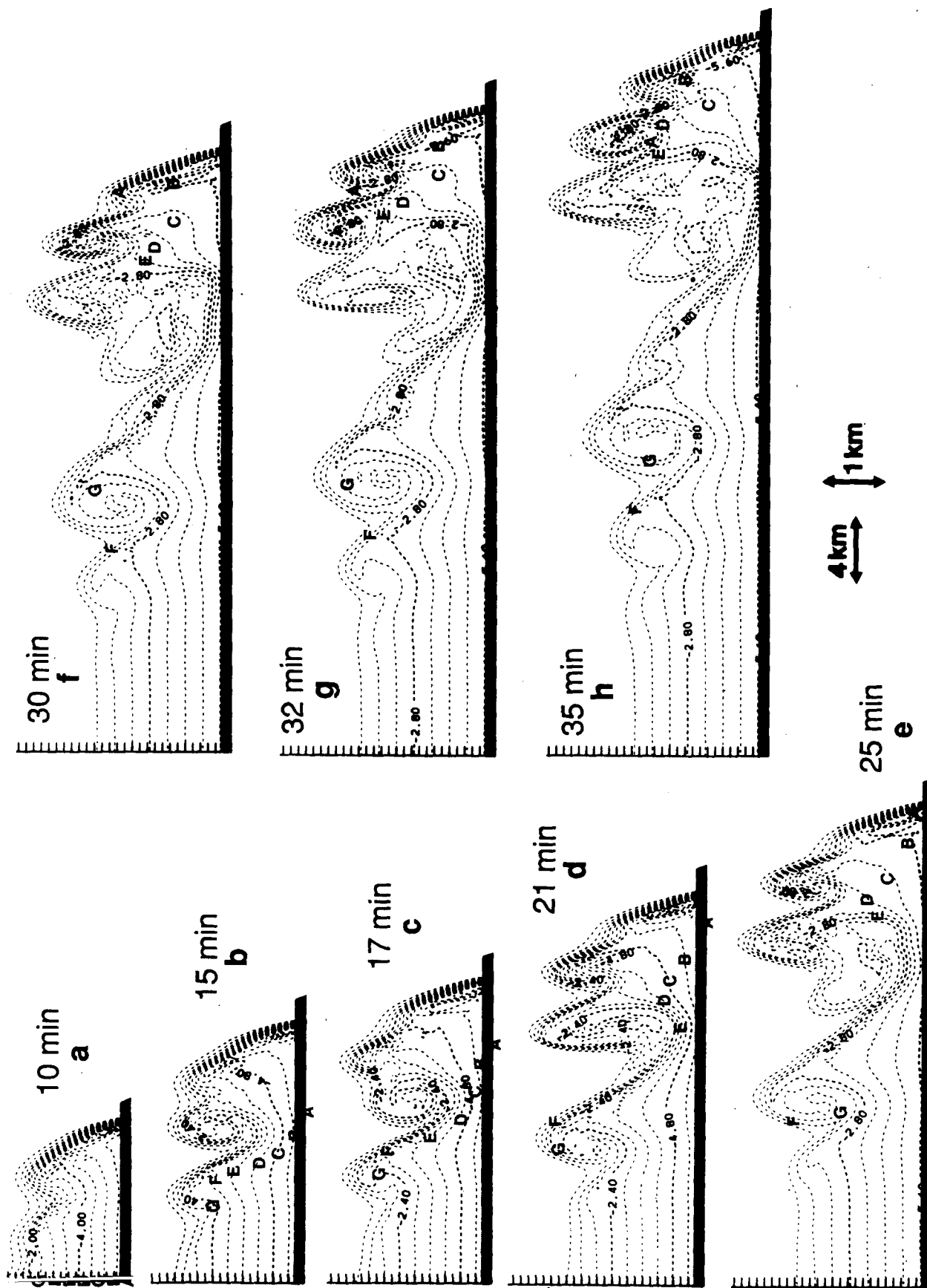
FIG. 13. A sequence describing the motion of seven air parcels (labeled A through G) in the interior of a simulated outflow. For reference, the perturbation potential temperature field is shown by the dashed contours (note the different vertical and horizontal scales). See the text for further details.

By 25 min (Fig. 13e), parcels D and E become entrained into the updraft of the billow conglomerate toward the rear of the outflow head. Meanwhile, parcel A reaches the gust front and begins a rapid ascent. At 30 min (Fig. 13f), parcel A has reached the upper portion of the outflow, and is beginning to circulate within the new billow forming there. Parcels B and C also continue moving upward, albeit at a much slower rate.

Throughout the remainder of the simulation (31 to 35 min), parcel A travels completely around the large KH billow atop the outflow head while B follows essentially the same pattern. Parcels C, D and E continue to rise under the influence of the internal head circulation, while F and G remain confined to the body of the outflow.

Numerous trajectories not presented here substantiate the patterns shown in Fig. 13, and also indicate that air in the vertical column immediately behind the gust front has its origin very close to the ground ($z = 0$ to 100 m). Therefore, as shown by parcel A in Fig. 13, air near the ground eventually overtakes the front and curves sharply upward behind the cold-air interface. Air further back within the outflow head (e.g., parcels B and C) may be traced to an origin 150 to 250 m above the ground in the body of the outflow, while parcels starting even higher (e.g., F and G) never reach the gust front.

To determine the origin of air within the various KH billows, several air parcels are placed in the regions of turbulence and then tracked backward in time. These computations indicate that most of the air within any particular billow comes from near the surface but somewhat upstream from the region of billow formation. Furthermore, environmental air above the outflow, which is entrained into the billow circulations, typically has its origin 100 to 500 m above the top of the cold pool.

An interesting aspect of the simulation in Fig. 13 is that, based on the horizontal distance between successive billows, there appear to be two distinct regimes of billow development: 1) immediately behind the gust front atop the outflow head, and 2) within the body of the outflow, well upstream from the head. The billows near the outflow head are narrower in lateral extent, are spaced closer together, and grow to a larger amplitude than the billows upstream. One explanation for this behavior is that the shear layer atop the outflow in the *body* region behaves much like an unbounded vortex sheet, i.e., nearly parallel shear flow, whereas *closer to the front,* the sheet is continually perturbed by flow up and over the outflow head, thereby giving a preferred scale to the billows. In addition, a coupling of circulations is taking place at the outflow head (i.e., the circulations associated with the KH billows are superimposed on the larger, internal solenoidal circulation), thereby giving rise to a billow structure at the head which is different from that observed upstream.

Since observational data on outflows is often in the form of time series analyses from surface-based instruments, it is instructive to view numerical model data in the same format. Figure 14 shows time series plots of the horizontal velocity v (m s^{-1}), perturbation pressure P' (mb), and perturbation potential temperature θ' (K) at the surface for the simulation in Fig. 13. The point of measurement is 16 km from the cold-air source region (which is approximately the position of the gust front in Fig. 13c).

The approach of the gust front is heralded by a gradual increase in surface pressure (which was shown in section 3a to be nonhydrostatic) and wind speed. As the front passes, the surface temperature (pressure) drops (rises) and the horizontal wind speed increases markedly. While the temperature deficit remains fairly constant thereafter, large amplitude fluctuations in both the wind speed and pressure are observed, and are coincident with the passage of a large KH billow overhead (the wind speed increase is due to a rapid downward transfer of momentum by the billow, while the pressure drop is associated with the cyclostrophic effect discussed in section 3b). Following the passage of this billow, all fields attain a quasi-steady state. A remarkably similar pattern in the surface pressure and temperature fields was noted by Mueller and Carbone (1986) for an observed outflow which also contained KH billows.

2) EXTERNAL FLOW STRUCTURE

In order to document the destiny of environmental air approaching the gust front, trajectory calculations are performed by placing several air parcels in a 5 km tall vertical stack a distance of 3 km ahead of the gust front. Parcels in the lowest 100 m of the stack are initially 10 m apart, while those above have an initial separation of 100 m. The parcels are released 15 min into the simulation, by which time the gust front is sufficiently removed from possible contaminating influences of the lateral boundary.

Figure 15 shows a plot of the total vertical distance traveled by the parcels as a function of their initial starting height. The erratic nature of the curve for parcels originating below $z = 0.25$ km is a reflection of this air's entrainment by KH billows developing at the gust front. The curve is quasi-linear for parcels up to $\sim$3 km, at which point the distance traveled reaches a constant value of $\sim$1.5 km. These results agree qualitatively with trajectories presented by Seitter (1983) for a dry outflow simulation and also resemble trajectories from observations and for potential flow over an ellipsoid (Foote, 1984).

A detailed examination of numerous air parcels approaching the outflow indicates that air in the lowest 2 km of the boundary layer closely follows the outline of the cold-air pool as it passes over the gust front and through the regions of KH instability. Parcels originating above 2 km pass over the outflow and do not
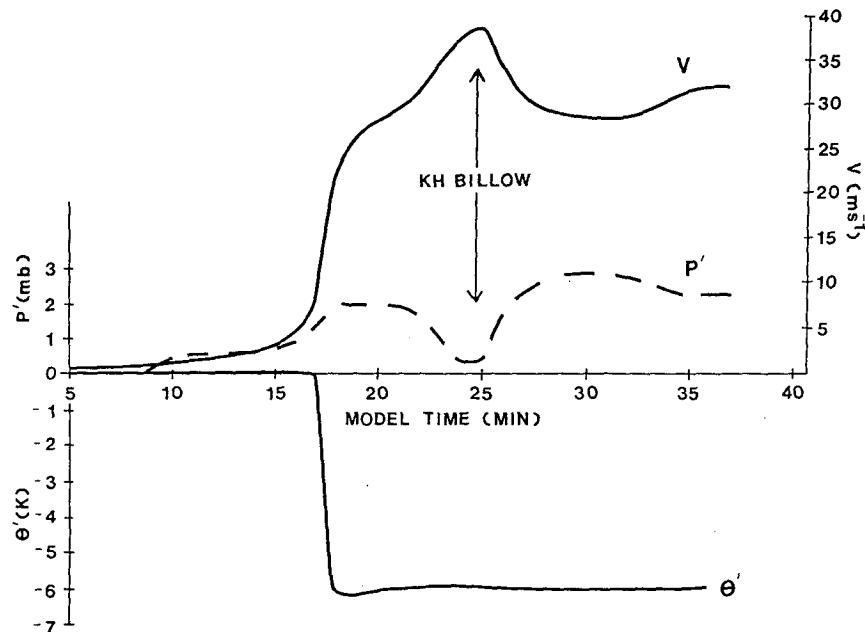
FIG. 14. Time series plots of the surface horizontal velocity v (m s^{-1}), perturbation pressure P' (mb), and perturbation potential temperature θ' (K) for the simulation in Fig. 13. The point of measurement is 16 km from the cold-air source region (approximately the position of the gust front in Fig. 13c).

become entrained into the top of the cold pool. Obviously these trajectories would change if condensation were allowed to occur in the model (e.g., Droegemeier and Wilhelmson, 1985a).

c. Impact of numerical smoothing on KH instability

The onset of KH instability is predicated on the magnitude of the local fluid shear, i.e., the Richardson number (e.g., Chandrasekhar, 1961). Therefore, one must be particularly certain that this shear is properly represented in a numerical model where smoothing occurs both explicitly (eddy diffusion) and implicitly
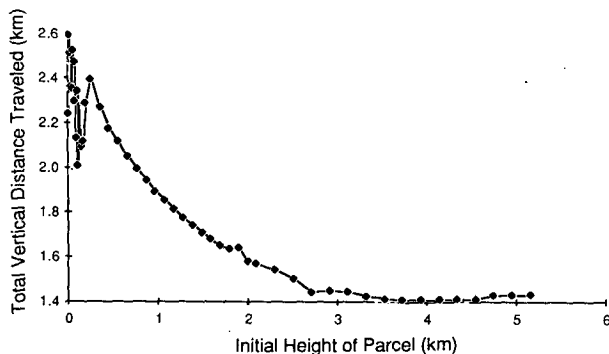

FIG. 15. The total vertical distance traveled by several air parcels released in a 5 km tall vertical stack at $t = 15$ min and 3 km ahead of the gust front in Fig. 13.

(finite difference averaging). In this section we examine how computational diffusion affects the KH instability in our modeled outflows, and recommend potential solutions for dealing with this issue in computational fluid dynamics.

Figure 16 shows the perturbation potential temperature at 20 min for an outflow identical to the control case of Fig. 12, but with a horizontal smoothing coefficient three times as large ($K_y = 300$ m^2 s^{-1}). In general, the KH billows are similar in structure, except that the overall flow field implied by the isentropes in Fig. 16 is somewhat smoother than in Fig. 12 (particularly in the horizontal). Results from these and other experiments suggest that KH instability in these outflows is not overly sensitive to the magnitude of the horizontal smoothing, provided that $K_y \leq 300$ m^2 s^{-1}. This result is not unexpected since the physical basis of KH instability lies in the *vertical* gradients of density and horizontal velocity.

To determine the sensitivity of KH instability to *vertical* smoothing, we examine simulations in which the vertical and horizontal smoothing coefficients are equal. Figure 17a shows an experiment with $K_y = K_z = 50$ m^2 s^{-1}. In this case, only one overturning wave is present behind the outflow head (compare results of section 2). Since $K_y \ll 300$ m^2 s^{-1}, the suppression of KH instability in this case results from increased vertical smoothing, i.e., smearing of the vertical shear layer causes the Richardson number to lie well above the critical value of 0.25. By further increasing the magnitude of the smoothing coefficients (Figs. 17b–d),
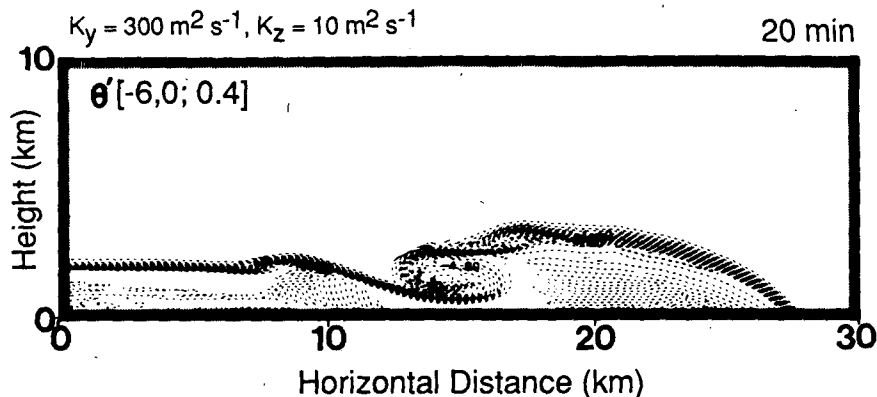
FIG. 16. The perturbation potential temperature at 20 min for a simulation identical to that in Fig. 12, but with a horizontal computational smoothing coefficient three times as large (K_y = 300 m^2 s^{-1}).

we nearly suppress all overturning in the simulated outflows (note that the large diffusion used in earlier experiments, e.g., Figs. 7, 8 and 10, prevented the formation of KH billows). Therefore, it appears that with present numerical techniques, one must choose the background damping carefully so that only the smallest-scale, aliasing-induced waves are damped.

It is important to note that, in addition to removing aliased energy from the smallest resolvable scales of motion, the "background" damping serves to maintain the finite width of the cold-air interface. To clarify this point, note that when an outflow moves through the neutral environment in these experiments, it is the fastest propagating signal in the domain (i.e., the gravity wave phase speed is zero). Thus, the flow is "supercritical," and the outflow represents a shock front *with respect to gravity wave motion*. In the absence of any diffusion, the front would collapse to an unresolvable contact discontinuity.

It is appropriate at this point to comment on our use of different mixing coefficients in each coordinate direction. There are several reasons why such an approach is *not* dynamically consistent. For example, it is impossible to formulate a vorticity equation when $K_y \neq K_z$ because the velocity still appears as a dependent variable. In addition, one typically thinks of turbulent mixing as being homogeneous and isotropic. Therefore, our justification for allowing K_y to differ from K_z is based not on dynamical considerations, but rather on model results.

There exist a number of alternative approaches for treating turbulence explicitly in numerical models. In addition to using very high spatial resolution, one might choose to employ a numerical interface technique (e.g., Norman, 1980; Norman et al., 1983, 1984; Smith et al., 1984) to accurately track the boundary between the cold outflow air and the warmer ambient environment. In addition, the Marker and Cell (MAC) technique is quite popular for handling interfaces (e.g.,

Harlow and Welch, 1965; Amsden and Harlow, 1970), although it typically requires inordinate amounts of computer time and can be very difficult to program. The most promising alternative at this point appears to be the piecewise parabolic method (PPM: Woodward, 1983; Colella and Woodward, 1984), and efforts are underway to explore its applicability in outflow, microburst, and cloud modeling studies.

d. The role of the Reynolds number in outflow modeling

Up to this point, we have been freely comparing the numerical model results with laboratory density currents. Given, however, that the Reynolds number (Re) varies by five to eight orders of magnitude between laboratory and atmospheric flows, one is led to ask: what flow regime (i.e., Reynolds number) are we simulating in the model? This is a crucial question since, strictly speaking, the outflow model represents neither the laboratory environment nor the real atmosphere.

The lack of explicit eddy viscosity in the outflow model implies that the Reynolds number is infinitely large. If, however, we compute a Reynolds number for the simulated outflows using the background mixing coefficients in place of the kinematic viscosity, we find that Re $\sim 10^2$ to 10^3. Since these values are representative of laboratory flows, but are several orders of magnitude smaller than those found in the atmosphere, it is unclear which physical system the model represents.

To address this issue, recall from section 2 that the dynamical similarity between outflows and density currents is based not upon equality of the Reynolds number, but rather upon the internal densimetric Froude number. Furthermore, as shown by Simpson and Britter (1980), many features common to both laboratory and atmospheric density currents are independent of the Reynolds number, and thus one

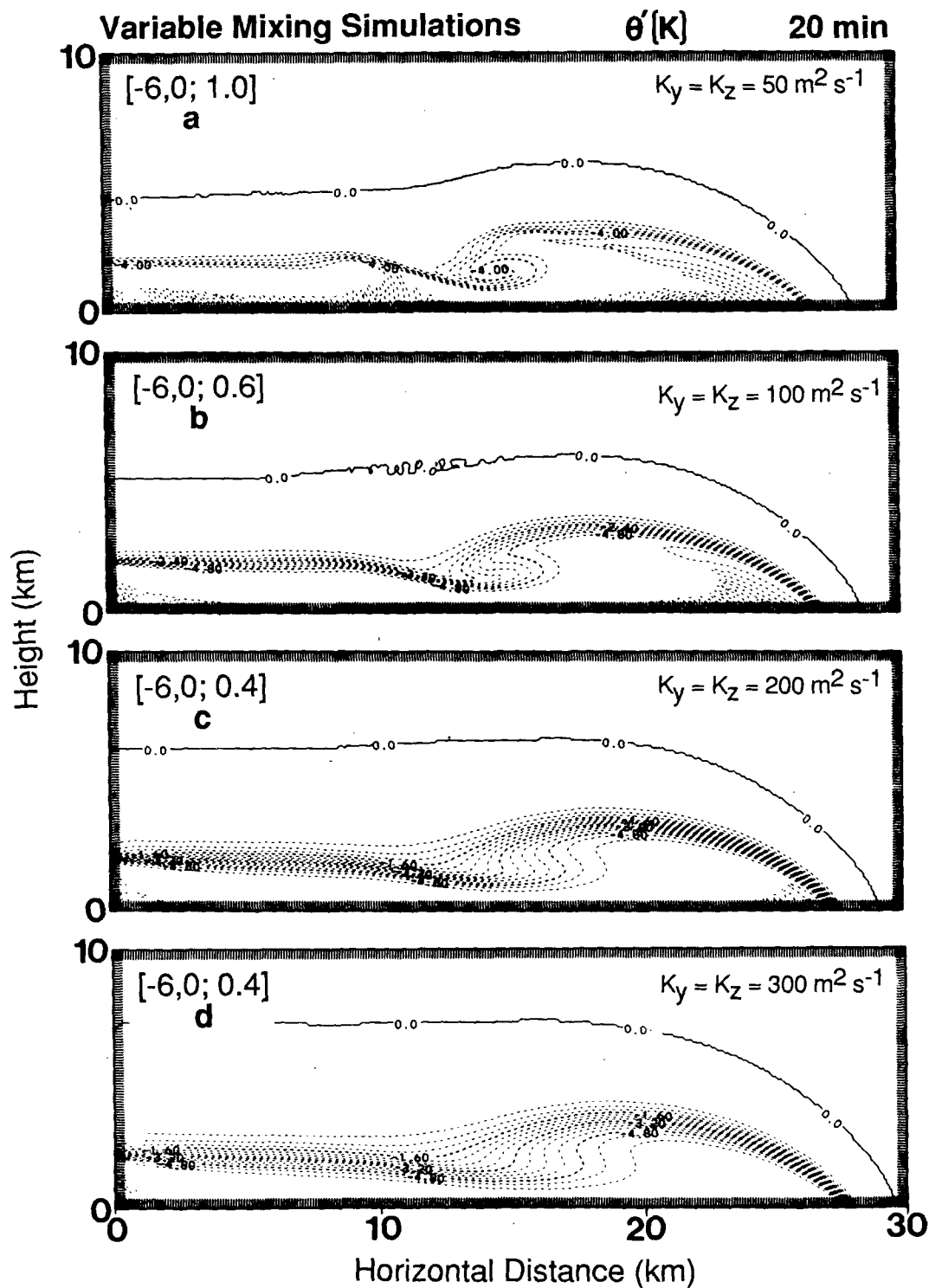**Variable Mixing Simulations** θ'[K]   **20 min**

FIG. 17. As in Fig. 15 but for the mixing coefficients shown in the upper right corner of each panel (note the different contour interval in each panel).

might be tempted to respond that the model does indeed represent the atmosphere.

Although the above reasoning seems fairly sound, it is seriously limited because it fails to consider that, in contrast to laboratory and atmospheric flows, the outflow model does not represent a continuum, i.e., results

of a numerical grid point model always depend to some degree upon the spatial resolution. To illustrate this point, we note that the large difference in Reynolds number between *laboratory and atmospheric* density currents is due primarily to a geometric scale difference. In contrast, the large difference in Reynolds number between *modeled and atmospheric* density currents (which have the same physical scale) results from a difference in kinematic viscosity. For example, in computing a Reynolds number for an observed outflow, one uses the kinematic viscosity of air $v \sim 10^{-5}$ m^2 s^{-1}. In the outflow model, however, this viscosity must be replaced by the numerical damping coefficient $K \sim 10^2$ m^2 s^{-1}. Therefore, in order to provide for atmospheric Reynolds numbers in a laboratory tank experiment, one need only build a larger apparatus or use a less viscous fluid. In contrast, the only way to obtain an atmospheric Reynolds number regime in the outflow model is to decrease the magnitude of the mixing coefficients. In order to avoid nonlinear instability, this decrease in smoothing must be accompanied by a corresponding decrease in the model's grid size. Although this implies that extremely high resolution (10 to 40 m) is needed to accurately model outflows, the results in Fig. 12 suggest that many features, particularly turbulent mixing, can be modeled with coarser resolution in the laboratory Reynolds number regime.

To illustrate the influence of grid resolution on simulated outflows, Fig. 18 shows the perturbation potential temperature at 20 min for outflows simulated with three different grid sizes. For uniformity in comparison, the computational smoothing rate [i.e., $K_y \Delta t/(\Delta y)^2$ and $K_z \Delta t/(\Delta z)^2$] is the same in each experiment. The outflow in panel a is the control experiment discussed in section 4a (100 m grid), while in panel b, the model grid spacing is 200 m. In the latter case, the model is able to represent only the large breaking wave behind the outflow head, while the billow forming in the body of the outflow in panel a is completely absent. When the grid resolution is further degraded to 500 m (Fig. 18c), only an ill-defined breaking wave is present behind the outflow head. At this low resolution, the model is completely unable to represent any aspect of KH instability atop the cold-air pool. These results suggest that, while 500 m grid resolution is quite adequate for most types of cloud modeling, it is completely unsuitable for explicitly representing the turbulent structure of outflows.

5. Summary and outlook

In this first paper of a two-part series, a dry, two-dimensional, slab-symmetric numerical model was developed and used to investigate the dynamics of thunderstorm outflows. Our key objective was to simulate outflows with nearly inviscid equations and high spatial resolution in an effort to resolve, rather than parameterize, physically important processes such as turbulent mixing.

To provide flexibility in the model code, a fully prognostic system of equations was used. The time step limitation imposed by acoustic waves was overcome by reducing the sound wave phase speed. This "quasi-compressibility" approximation was evaluated quantitatively by comparing simulations from the quasi-compressible outflow model (QCOM) with a fully compressible version (FCOM). For the types of flows being considered, the QCOM was found to produce solutions qualitatively and quantitatively similar to those of the FCOM, provided that the imposed sound speed was "sufficiently large" (i.e., approximately twice the speed of the fastest physical mode in the model).

To facilitate interpretation of the model results, and to allow for more direct comparison with laboratory density currents, all simulations were conducted in a calm, dry adiabatic atmosphere. The outflows were initialized as horizontally-propagating pools of cold air having a specified vertical temperature profile, depth, and temperature deficit. By holding two of these parameters fixed while varying the third, we established relationships among these physically important variables. In particular, we found that the outflow head depth was controlled by the internal temperature distribution via solenoidal effects. In addition, due to vorticity and hydrostatic pressure considerations, temperature advection by the internal gust front circulation was found to play a key role in determining the frontal propagation speed. A dynamically-induced pressure ridge was noted to precede the frontal interface, in agreement with previous observational studies.

As has been the case in numerous laboratory density current studies, internal densimetric Froude numbers calculated for the modeled outflows varied widely depending upon the method of computation. In general, these values were somewhat smaller than predicted by theory, yet much larger than typically found in atmospheric density currents.

The pressure field in the modeled outflows was found to contain a significant rotationally induced component (in addition to the hydrostatic portion) immediately behind the outflow head. This feature may be responsible for surface pressure drops and local wind surges which often occur several minutes after gust front passage.

By using high spatial resolution, and with a judicious choice for the numerical smoothing coefficients, we found that the model was capable of simulating the explicit turbulent structure of outflows. In particular, this turbulence was manifest as billows or lateral vortex rolls resulting from Kelvin–Helmholtz shearing instability. These billows typically originated near the outflow head just above the gust front, and then grew in amplitude while traveling upstream relative to the front. The growth rates, horizontal wavelengths, and conditions for onset of the modeled eddies were found to agree with linear theory and laboratory density currents. However, due to its two-dimensionality, the nu-
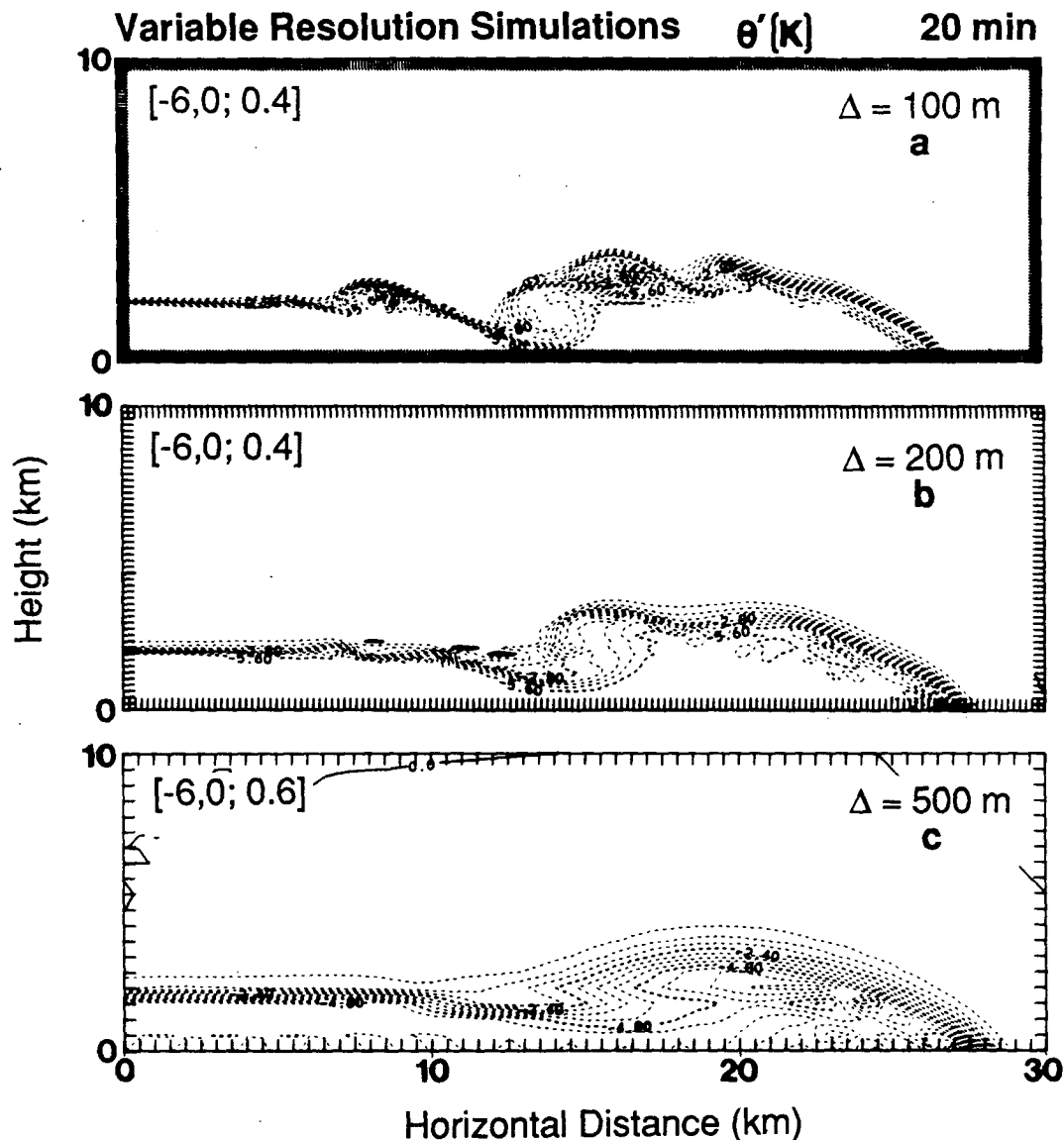
FIG. 18. The perturbation potential temperature at 20 min for simulations with (a) a 100 m grid, (b) a 200 m grid, and (c) a 500 m grid. Panel a is the control simulation in Fig. 12 (note the different contour interval in each panel).

merical model was unable to capture the ultimate breakdown of the billows into small-scale turbulence.

Time-dependent air parcel trajectories were utilized to examine the kinematics of the simulated outflows. We showed that near-surface air in the body of the outflow accelerated rapidly and eventually overtook the front, while air higher up became entrained into the developing KH billows and never entered the head region. Trajectories of environmental parcels passing up and over the outflow were found to agree with observations, and with ideal flow over a solid obstacle.

The KH instability in the modeled outflows was shown to be quite sensitive to both the magnitude of the vertical computational smoothing coefficient and

to the spatial grid resolution. Excessive smoothing artificially "smeared" the vortex sheet atop the cold-air pool, thereby preventing the onset of KH instability. Use of such excessive vertical smoothing may explain why previous outflow modeling studies have shown no evidence of KH waves. Adequate spatial resolution, shown here from similarity principles to be essential for modeling outflows, has been lacking in previous modeling efforts, and may provide additional evidence for the absence of KH billows in those studies.

Part II of this paper will address the effects of ambient wind shear and static stability on modeled outflow dynamics. In particular, we will focus on how these parameters influence turbulent mixing, outflow depth and

propagation speed, and the ability of a gust front to trigger deep convective clouds.

Although the results described herein are obviously limited by the two-dimensionality of the numerical model, we feel they nevertheless lend insight into the basic features of real outflows. With the advent of extremely large-capacity, fast-access memory supercomputers, we are now implementing fully three-dimensional models using high spatial resolution (50 to 100 m) and detailed microphysics. Such models will hopefully be able to address the long-standing question of lobe and cleft mixing in density currents, along with the partitioning of energy into various scales of the flow.

6. Supplement: Visualization of outflows and density currents

The highly time-dependent nature of thunderstorm outflows and laboratory density currents poses a difficult problem for flow visualization using only static drawings. To overcome this problem, we recently produced a five-minute color movie entitled: Numerical Simulation of a Thunderstorm Outflow and Comparison with Laboratory Density Currents. In it, we utilize a split-screen presentation to facilitate comparison between the laboratory and numerically simulated flows, and we depict the details of the model flow field by tracking several thousand colored tracer particles throughout the domain. Spatial correlations between structures in the scalar and momentum fields (e.g., the Kelvin–Helmholtz billows, the pressure jump preceding the gust front) are also documented using multiple window presentations.

Copies of this movie in video or 16 mm format are available from the authors upon request. The movie was produced on the Cray X-MP at Digital Productions (a division of Omnibus Simulation, Inc.), Los Angeles under support from National Science Foundation Grant ATM-8415222.

APPENDIX

Derivation of the Frequency Equation (10)

To derive the frequency equation (10), we linearize the gravity and sound wave terms in the nonlinear model equations (4)–(7) by writing the dependent variables in terms of a vertically stratified, motionless, hydrostatic basic state (denoted by an overbar), and a small deviation from it (indicated by a prime):

$$v = v'(y, z, t)$$
$$w = w'(y, z, t)$$
$$\theta = \bar{\theta}(z) + \theta'(y, z, t)$$
$$\pi = \bar{\pi}(z) + \pi'(y, z, t)$$
$$\frac{d\bar{\pi}}{dz} = -g/(C_p\bar{\theta}). \tag{A1}$$

Substituting (A1) into (4)–(7) yields the following set of linearized equations:

$$\frac{\partial v'}{\partial t} + C_p\bar{\theta}\frac{\partial \pi'}{\partial y} = 0 \tag{A2}$$

$$\frac{\partial w'}{\partial t} + C_p\bar{\theta}\frac{\partial \pi'}{\partial z} - g\frac{\theta'}{\bar{\theta}} = 0 \tag{A3}$$

$$\frac{\partial \theta'}{\partial t} + w'\frac{d\bar{\theta}}{dz} = 0 \tag{A4}$$

$$\beta\frac{\partial \pi'}{\partial t} + \frac{c_s^2}{C_p\bar{\theta}}\left\{\frac{\partial v'}{\partial y} + \frac{1}{\bar{\rho}}\frac{\partial}{\partial z}(\bar{\rho}w')\right\} + \frac{c_s^2}{C_p\bar{\theta}^2}w'\frac{d\bar{\theta}}{dz} = 0 \tag{A5}$$

where β is a tracer used in the subsequent analysis.

Since the coefficients in (A2)–(A5) are functions of height, we solve for the vertical structure by seeking normal mode solutions of the form

$$\begin{bmatrix} v' \\ w' \\ \theta' \\ \pi' \end{bmatrix} = \begin{bmatrix} V \\ W \\ T \\ P \end{bmatrix} e^{i(ly+mz-\sigma t)-Nz} \tag{A6}$$

where V, W, T and P are real amplitudes. In addition, σ, l and m are the frequency, horizontal wavenumber and vertical wavenumber, respectively (also assumed to be real), and N is a constant that must be determined. Substituting (A6) into (A2) to (A5) yields a set of four homogeneous linear algebraic equations which may be written in matrix notation as

$$
\begin{bmatrix}
-\sigma & 0 & 0 & C_p\bar{\theta}l \\
0 & -i\sigma & -g/\bar{\theta} & C_p\bar{\theta}(im-N) \\
0 & d\bar{\theta}/dz & -i\sigma & 0 \\
\dfrac{c_s^2 il}{C_p\bar{\theta}} & \dfrac{c_s^2}{C_p\bar{\theta}}\left[(im-N)+\dfrac{d\ln\bar{\rho}}{dz}+\dfrac{d\ln\bar{\theta}}{dz}\right] & 0 & -i\beta\sigma
\end{bmatrix}
\begin{bmatrix} V \\ W \\ T \\ P \end{bmatrix}
=
\begin{bmatrix} 0 \\ 0 \\ 0 \\ 0 \end{bmatrix}
\quad\text{(A7)}
$$

For a nontrivial solution, the determinant of the coefficient matrix in (A7) must vanish. Performing this operation yields

$$
N = \frac{S_\rho + S_\theta}{2} \quad\text{(A8)}
$$

and

$$
\beta\sigma^4 - \sigma^2\left[c_s^2(l^2+m^2)+g\beta S_\theta+\frac{c_s^2(S_\rho+S_\theta)^2}{4}\right] + c_s^2 l^2 g S_\theta = 0 \quad\text{(A9)}
$$

where $S_\theta = d\ln\bar{\theta}/dz$ and $S_\rho = d\ln\bar{\rho}/dz$.

Equation (A9) is the frequency equation for mixed sound–gravity waves for the linear system (A2)–(A5), and is identical to Eq. (10) in the text.

REFERENCES

Achtemeier, G. L., 1982: A semi-Lagrangian gust-front model. *Preprints, 12th Conf. on Severe Local Storms*, San Antonio, Amer. Meteor. Soc., 131–134.

Addis, R. P., 1984: A numerical model of surface outflows from convective storms. *Bound.-Layer Meteor.*, **28**, 121–160.

Amsden, A. A., and F. H. Harlow, 1970: The SMAC method—a numerical technique for calculating incompressible fluid flows. Los Alamos Scientific Laboratory Report LA-4370, 85 pp.

Anderson, J. R., K. K. Droegemeier and R. B. Wilhelmson, 1985: Simulation of the thunderstorm subcloud environment. *Preprints, 14th Conf. on Severe Local Storms*, Indianapolis, Amer. Meteor. Soc., 147–150.

Asselin, R., 1972: Frequency filter for time integrations. *Mon. Wea. Rev.*, **100**, 487–490.

Benjamin, T. B., 1968: Gravity currents and related phenomena. *J. Fluid Mech.*, **31**, 209–248.

Blumen, W., 1984: An observational study of instability and turbulence in nighttime drainage winds. *Bound. Layer Meteor.*, **28**, 245–269.

Brandes, E. A., 1977: Gust front evolution and tornado genesis as viewed by Doppler radar. *J. Appl. Meteor.*, **16**, 333–338.

——, 1981: Fine structure of the Del City-Edmond tornadic mesocirculation. *Mon. Wea. Rev.*, **109**, 635–647.

——, 1984: Vertical vorticity generation and mesocyclone sustenance in tornadic thunderstorms: The observational evidence. *Mon. Wea. Rev.*, **112**, 2253–2269.

Britter, R. E., and J. E. Simpson, 1978: Experiments on the dynamics of a gravity current head. *J. Fluid Mech.*, **88**, 223–240.

——, and ——, 1981: A note on the structure of the head of an intrusive gravity current. *J. Fluid Mech.*, **112**, 459–466.

Brown, G. L., and A. Roshko, 1974: On density effects and large structure in turbulent mixing layers. *J. Fluid Mech.*, **64**, 775–816.

Chandrasekhar, S., 1961: *Hydrodynamic and Hydromagnetic Stability*, Oxford Press, Ch. XI, 481–514.

Charba, J., 1974: Application of a gravity current model to analysis of squall line gust front. *Mon. Wea. Rev.*, **102**, 140–156.

Chen, C.-S., 1980: The effect of the gust front on the generation of

new convection. Ph.D. thesis, Dept. of Atmos. Sci., University of Illinois, 192 pp.

Chorin, A. J., 1967: A numerical method for solving incompressible viscous flow problems. *J. Comput. Phys.*, **2**, 12–16.

Colella, P., and P. R. Woodward, 1984: The piecewise parabolic method (PPM) for gas-dynamical calculations. *J. Comput. Phys.*, **54**, 174–201.

Crook, N. A., and M. J. Miller, 1985: A numerical and analytical study of atmospheric undular bores. *Quart. J. Roy. Meteor. Soc.*, **111**, 225–242.

Daly, B. J., and W. E. Pracht, 1968: Numerical study of density current surges. *Phys. Fluids*, **11**, 15–30.

Deardorff, J. W., 1975: The development of boundary-layer turbulence models for use in studying the severe storm environment. Proc. SESAME Meeting, Boulder, NOAA-ERL, 251–264.

Didden, N., and T. Maxworthy, 1982: The viscous spreading of plane and axisymmetric gravity currents. *J. Fluid Mech.*, **121**, 27–42.

Donn, W. L., P. L. Milic and P. Brilliant, 1956: Gravity waves and the tropical sea-breeze. *J. Meteor.*, **18**, 356–361.

Drazin, P. G., 1958: The stability of a shear layer in an unbounded heterogeneous inviscid fluid. *J. Fluid Mech.*, **4**, 214–224.

Droegemeier, K. K., 1985: *The numerical simulation of thunderstorm outflow dynamics*. Ph.D. thesis, Dept. of Atmos. Sci., University of Illinois, 695 pp.

——, and R. B. Wilhelmson, 1985a: Three-dimensional numerical modeling of convection produced by interacting thunderstorm outflows. Part I: Control simulation and low-level moisture variations. *J. Atmos. Sci.*, **42**, 2381–2403.

——, and ——, 1985b: Three-dimensional numerical modeling of convection produced by interacting thunderstorm outflows. Part II: Variations in vertical wind shear. *J. Atmos. Sci.*, **42**, 2404–2414.

——, and ——, 1985c: Kelvin–Helmholtz instability in a numerically simulated thunderstorm outflow. *Preprints, 14th Conf. on Severe Local Storms*, Indianapolis, Amer. Meteor. Soc., 151–154.

Eckart, C., 1960: *Hydrodynamics of Oceans and Atmospheres*. Pergamon Press, 290 pp.

Emmitt, G. D., 1985: Convective storm downdraft outflows detected by NASA/MSFC's airborne 10.6 μm pulsed Doppler radar system. NASA Contractor Report CR-3898, 46 pp.

Farquharson, J. S., 1937: Haboobs and instability in the Sudan. *Quart. J. Roy. Meteor. Soc.*, **63**, 393–414.

Foote, G. B., 1984: Influence of gust fronts on the propagation of storms. Proc., Ninth Int. Cloud Physics Conf., Tallin, 419–422.

Fulton, R. A., and D. S. Zrnić, 1985: Structure of a thunderstorm outflow from single Doppler radar observations. *Preprints, 14th Conf. on Severe Local Storms*, Indianapolis, Amer. Meteor. Soc., 73–76.

Georgi, J., 1937: Pampero secco vom 17 Jul; 1935. *Der Seewart*, **7**, 199–205.

Goff, R. C., 1975: Thunderstorm outflow kinematics and dynamics. NOAA Tech. Memo ERLTM-NSSL, No. 75, 63 pp.

——, 1977: Some observations of thunderstorm-induced low-level wind variations. *J. Aircraft*, **14**, 423–427.

Harlow, F. H., and J. E. Welch, 1965: Numerical calculation of time-dependent viscous incompressible flow. *Phys. Fluids*, **8**, 21–82.

Holle, R. L., and M. W. Maier, 1980: Tornado formation from downdraft interaction in the FACE mesonetwork. *Mon. Wea. Rev.*, **108**, 1010–1028.

Holton, J. R., 1979: *An Introduction to Dynamical Meteorology*, 2nd ed., Academic Press, 391 pp.

Huppert, H. E., 1982: The propagation of two-dimensional and axisymmetric viscous gravity currents over a rigid horizontal surface. *J. Fluid Mech.*, **121**, 43–58.

Kao, T., C. Park and H.-P. Pao, 1978: Inflows, density currents, and fronts. *Phys. Fluids*, **21**, 1912–1922.

Keulegan, G. H., 1957: Thirteenth progress report on model laws for density currents: An experimental study of the motions of saline water from locks into fresh water channels. NBS Report 5168, 21 pp.

——, 1958: Twelfth progress report on model laws for density currents: The motion of saline fronts in still water. NBS Report 5831, 29 pp.

Klaassen, G. P., and T. L. Clark, 1985: Dynamics of the cloud-environment interface and entrainment in small cumuli: Two-dimensional simulations in the absence of ambient shear. *J. Atmos. Sci.*, **42**, 2621–2642.

Klemp, J. B., and D. K. Lilly, 1978: Numerical simulation of hydrostatic mountain waves. *J. Atmos. Sci.*, **35**, 78–107.

——, and R. Rotunno, 1983: A study of the tornadic region within a supercell thunderstorm. *J. Atmos. Sci.*, **40**, 359–377.

——, and R. B. Wilhelmson, 1978: The simulation of three-dimensional convective storm dynamics. *J. Atmos. Sci.*, **35**, 1070–1096.

Klingle, D. L., 1985: A gust front case studies handbook. MIT Lincoln Laboratory Project Report ATC-129, 108 pp.

Koch, S. E., 1984: The role of an apparent mesoscale frontogenetical circulation in squall line initiation. *Mon. Wea. Rev.*, **112**, 2090–2111.

Lilly, D. K., 1965: On the computational stability of numerical simulations of time-dependent nonlinear geophysical fluid dynamics problems. *Mon. Wea. Rev.*, **93**, 11–26.

McCaul, E. W., 1985: *Observations of Oklahoma Convection using airborne Doppler lidar and ground-based Doppler radar.* M.S. thesis, University of Oklahoma, School of Meteorology, 320 pp.

Middleton, G. V., 1966: Experiments on density and turbidity currents. *Can. J. Earth Sci.*, **3**, 523–546.

Miles, J. W., and L. N. Howard, 1964: Note on a heterogeneous shear flow. *J. Fluid Mech.*, **20**, 331–336.

Miller, L. J., and J. C. Fankhauser, 1983: Radar echo structure, air motion and hail formation in a large stationary multicellular thunderstorm. *J. Atmos. Sci.*, **40**, 2399–2418.

Mitchell, K. E., and J. B. Hovermale, 1977: A numerical investigation of a severe thunderstorm gust front. *Mon. Wea. Rev.*, **105**, 657–675.

Mueller, C. K., and R. E. Carbone, 1986: Dynamics of a thunderstorm outflow. *J. Atmos. Sci.* (in press).

Norman, M. L., 1980: A numerical study of rotating interstellar clouds: Equilibrium and collapse. Ph.D. thesis, University of California and Lawrence Livermore Laboratory, Report URCL-52946, 223 pp.

——, K.-H. A. Winkler and L. Smarr, 1983: Propagation and morphology of pressure-confined supersonic jets. Max Planck Institute Report MPA-61, 24 pp.

——, L. Smarr and K.-H. Winkler, 1984: Fluid dynamical mechanisms for knots in astrophysical jets. Max Planck Institute Report MPA-115, 45 pp.

Ogura, Y., and J. G. Charney, 1962: A numerical model of thermal convection in the atmosphere. *Proc. Inter. Symp. Numerical Weather Prediction*, Tokyo, 7–13 November 1980, Meteor. Soc. Japan, 431–451.

Peterson, R. E., 1984: A triple-Doppler radar analysis of a discretely propagating multicell convection storm. *J. Atmos. Sci.*, **41**, 2973–2990.

Purdom, J. F. W., 1976: Some uses of high-resolution GOES imagery in the mesoscale forecasting of convection and its behavior. *Mon. Wea. Rev.*, **104**, 1474–1483.

——, 1979: The development and evolution of deep convection. *Preprints, 11th Conf. on Severe Local Storms*, Kansas City, Amer. Meteor. Soc., 143–150.

——, 1982: Subjective interpretation of geostationary satellite data for nowcasting. *Nowcasting*, Keith Browning, Ed., Academic Press, 149–156.

Robert, A. J., 1966: The integration of a low order spectral form of the primitive meteorological equations. *J. Meteor. Soc. Japan*, **44**, 237–245.

Rotunno, R., and J. Klemp, 1985: On the rotation and propagation of simulated supercell thunderstorms. *J. Atmos. Sci.*, **42**, 271–292.

Schlesinger, R. E., L. W. Uccellini and D. R. Johnson, 1983: The effects of the Asselin time filter on numerical solutions to the linearized shallow-water wave equations. *Mon. Wea. Rev.*, **111**, 455–467.

Schmidt, W., 1911: Zur Mechanik der Boen. *Z. Meteorol.*, **28**, 355–362.

Seitter, K. L., 1983: The effect of arc cloud generation on thunderstorm gust front motion. *Preprints, 13th Conference on Severe Local Storms*, Tulsa, Amer. Meteor. Soc., 249–252.

Simpson, J. E., 1969: A comparison between laboratory and atmospheric density currents. *Quart. J. Roy. Meteor. Soc.*, **95**, 758–765.

——, 1972: Effects of the lower boundary on the head of a gravity current. *J. Fluid Mech.*, **53**, 759–768.

——, D. A. Mansfield and J. R. Milford, 1977: Inland penetration of sea-breeze fronts. *Quart. J. Roy. Meteor. Soc.*, **103**, 47–76.

——, 1982: Gravity currents in the laboratory, atmosphere, and ocean. *Ann. Rev. Fluid Mech.*, **14**, 213–234.

——, and R. E. Britter, 1979: The dynamics of the head of a current advancing over a horizontal surface. *J. Fluid Mech.*, **94**, 478–497.

——, and ——, 1980: A laboratory model of an atmospheric mesofront. *Quart. J. Roy. Meteor. Soc.*, **106**, 485–500.

Simpson, J., N. E. Westcott, R. J. Clerman and R. A. Pielke, 1980: On cumulus mergers. *Arch. Meteor. Geophys. Bioklim.*, **A29**, 1–40.

Smagorinsky, J., 1963: General circulation experiments with the primitive equations: 1. The basic experiment. *Mon. Wea. Rev.*, **91**, 99–164.

Smith, M. D., M. L. Norman, K.-H. A. Winkler and L. Smarr, 1984: Hot spots in radio galaxies: A comparison with hydrodynamic simulations. Max Planck Institute Rep. MPA-150, 34 pp.

Soong, S.-T., and Y. Ogura, 1973: A comparison between axisymmetric and slab-symmetric cumulus cloud models. *J. Atmos. Sci.*, **30**, 879–893.

Stern, M. E., and L. J. Pratt, 1985: Dynamics of vorticity fronts. *J. Fluid Mech.*, **161**, 513–532.

Tao, W. K., and J. Simpson, 1984: Cloud interactions and merging: Numerical simulations. *J. Atmos. Sci.*, **41**, 2901–2917.

Teske, M. E., and W. S. Lewellen, 1977: Turbulent transport model of a thunderstorm gust front. *Preprints, 10th Conf. on Severe Local Storms*, Omaha, Amer. Meteor. Soc., 143–149.

Thorpe, A. J., M. J. Miller and M. W. Moncrieff, 1980: Dynamical models of two-dimensional downdraughts. *Quart. J. Roy. Meteor. Soc.*, **106**, 463–484.

Wakimoto, R. M., 1982: The life cycle of thunderstorm gust fronts as viewed with Doppler radar and rawinsonde data. *Mon. Wea. Rev.*, **110**, 1060–1082.

Weaver, J. F., and S. P. Nelson, 1982: Multiscale aspects of thunderstorm gust fronts and their effects on subsequent storm development. *Mon. Wea. Rev.*, **110**, 707–718.

Wilhelmson, R. B., and C.-S. Chen, 1982: A simulation of the development of successive cells along a cold outflow boundary. *J. Atmos. Sci.*, **39**, 1466–1483.

——, and J. B. Klemp, 1978: A numerical study of storm splitting that leads to long-lived storms. *J. Atmos. Sci.*, **35**, 1974–1986.

Woodward, P. R., 1983: Piecewise parabolic methods for astrophysical fluid dynamics. Lawrence Livermore National Laboratory Preprint No. UCRL-90009, 83 pp.

Yau, M. K., 1979: Perturbation pressure and cumulus convection. *J. Atmos. Sci.*, **36**, 690–694.

Young, G. S., and R. H. Johnson, 1984: Meso- and microscale features of a Colorado cold front. *J. Climate Appl. Meteor.*, **23**, 1315–1325.